

# Decoding the resolved star-formation history of galaxies with MUSE

Garreth Martin

20th April 2015

# Contents

<b>I Summary</b>	<b>4</b>
<b>II Initial Plan</b>	<b>5</b>
II.1 Plan submitted 21 <sup>st</sup> October 2014 . . . . .	5
II.2 Changes to the plan . . . . .	8
<b>1 Introduction</b>	<b>9</b>
1.1 Background and early approaches . . . . .	9
1.2 Stellar population synthesis . . . . .	11
1.2.1 SSPs . . . . .	11
1.3 Spectroscopic and photometric studies . . . . .	12
1.4 Reconstructing star formation history . . . . .	13
1.4.1 SED fitting . . . . .	13
1.4.2 Reddening due to dust . . . . .	16
1.4.3 Stellar kinematics . . . . .	19
1.4.4 Photometric and spectroscopic SED fitting . . . . .	20
1.5 Recovering star formation history with MUSE . . . . .	22
1.5.1 Test case: NGC 7742 . . . . .	22
<b>2 Data</b>	<b>22</b>
2.1 MUSE . . . . .	22
2.1.1 Errors . . . . .	23
2.2 GALEX . . . . .	23
2.2.1 Errors . . . . .	26
2.3 SDSS . . . . .	27
2.3.1 Errors . . . . .	29
2.4 Combined data . . . . .	31
2.5 Templates . . . . .	31
<b>3 Simple approach</b>	<b>34</b>
3.1 GANDALF . . . . .	34
3.2 Apertures . . . . .	35
3.3 Flux Densities . . . . .	38
3.4 Method . . . . .	40
3.4.1 Convolution of data . . . . .	40
3.4.2 Corrected Flux Densities . . . . .	44
3.4.3 Photometric fluxes . . . . .	47

<i>CONTENTS</i>	3
3.4.4 Additional Reddening . . . . .	49
3.5 MUSE spectrum only . . . . .	49
3.6 Photometry only . . . . .	53
<b>4 Extended Approach</b>	<b>56</b>
4.1 Results . . . . .	60
<b>5 Errors</b>	<b>62</b>
<b>6 Conclusion</b>	<b>67</b>
<b>References</b>	<b>70</b>

## I Summary

Reconstructing star-formation history is a crucial tool for understanding the evolution of galaxies. Astronomers are able to infer the star-formation properties of galaxies from multi-wavelength observations of the integrated light that is emitted. The spectral energy distribution of a galaxy is imprinted with the star formation history of that galaxy in terms of its principal stellar components, which can be recovered through SED fitting.

Galactic SEDs can consist of photometric data (average flux values within a discrete wavelength interval) or spectroscopic data (a continuous distribution of fluxes as a function of wavelength). Both photometric and spectroscopic forms of SED enjoy wide use in astronomy, however, there have been few attempts to combine these two types of data in the context of SED fitting (Chilingarian and Katkov, 2011).

A method for combining photometric and spectroscopic data in SED fitting was developed and tested. Spectroscopic data from MUSE was used in combination photometric data from GALEX and SDSS to recover the principle stellar components in the face-on starburst galaxy, NGC 7742. Apertures for the bulge, circum-nuclear ring and disk of NGC 7742 were extracted and used to explore star-formation history spatially across the galaxy.

Data was convolved with a Gaussian PSF in order that each image had a consistent angular resolution and the GANDALF (Sarzi et al., 2006) SED fitting code was modified. Alterations were made to calculate bandpass flux densities for the SSP templates and to include additional reddening for templates of age  $t \leq 10\text{Myrs}$ , which are subject to birth cloud attenuation.

The spectro-photometric approach was compared with SED fits utilising photometric SEDs and spectroscopic SEDs. It was found that purely photometric SEDs were not suitable for our purposes because they do not contain detail necessary to break reddening, age and metallicity degeneracies. When extrapolated into the UV, the spectroscopic SED fit was found to under or over-predict the observed UV flux density. The addition of GALEX data with the spectro-photometric approach allowed the model SED to be matched in the UV with the observed UV flux density, better constraining star formation history for young stellar populations, which are UV bright.

It is anticipated that this approach would be useful for mapping star-formation efficiency throughout galaxies. It may also have a more general use, allowing for more accurate SED fitting of limited spectra with the addition of more widely available photometric data.

## II Initial Plan

### II.1 Plan submitted 21<sup>st</sup> October 2014

#### Background

Modeling the spectral energy distribution (SED) of galaxies is essential for understanding the history of their star formation. The SED of a galaxy can be made of spectra providing a continuous distribution of fluxes as a function of wavelength or by a series of photometric data points, giving average flux values within discrete wavelength intervals (Walcher et al., 2010). Such SEDs can be fit to a library of stellar templates covering various ages and metallicities that have been treated according to dust attenuation, stellar kinematics and presence of gas emission in the galaxy (Walcher et al., 2010). This allows us to infer the principal stellar components of the galaxy and thus reconstruct star formation history. Historically, there has been a split between the use of optical spectra and broad-band photometry to reconstruct the star formation history of galaxies. Combining the two could have positive consequences for example, when only limited wavelength range spectra are available.

This project will focus on combining these two types of data within the GANDALF (Gas AND Absorption Line Fitting) fitting algorithm. I will use a combination of spectroscopic and photometric data to test and develop this approach. I have already altered the GANDALF code to use a combination of photometric and spectroscopic data for a Summer project, with promising preliminary results. During the course of this project, I will attempt to improve upon the existing results and investigate star formation history spatially across nearby galaxies. The focus will be on the spiral galaxy NGC7742, which is particularly interesting due to the fact that it is face-on and contains a super-position of young and old stellar populations. The code will need to be tested using different data sets and the limits of the approach established. The photometric and spectroscopic data will need to be correctly calibrated so that they match and errors will need to be carefully considered in order to establish the weight that should be assigned to each of the spectroscopic and photometric data points.

I will first need to calibrate the data. I will be using spectra from MUSE, an integral-field spectrograph installed on the VLT (Bacon et al., 2010) and photometry from the Hubble space telescope, the GALEX ultraviolet space telescope (Martin et al., 2005) and the Sloane Digital Sky Survey (SDSS), a spectroscopic survey using a 2.5m telescope. I will need to research the calibration of the data, filters used etc. Following this, I will be able to begin testing the code. This will involve testing the ability of the code to recover star formation history from synthetic data. The synthetic star

formation history will be created to mimic MUSE spectra with SDSS, GALEX and HST photometry. Testing will allow limits and errors to be quantified. After testing I will apply the combined spectroscopy and photometry approach to real data, including MUSE spectra with GALEX and MUSE spectra with HST observations of NGC7742.

## **Plan for report**

### 1. Introduction

- (a) Stellar populations and reconstructing star formation history of galaxies.
- (b) Background, early approaches (colour-colour).
- (c) Spectroscopic studies and simple stellar populations (SSPs).
- (d) SED fitting.
- (e) Introduce the idea of the project and original test case.

### 2. Data

- (a) Description of MUSE, HST, GALEX and SDSS data.
- (b)  $\lambda$  range, PSF, calibration.

### 3. Method

- (a) Implementation of the code.
- (b) Testing: limits, errors.

### 4. Application

- (a) Application to real data.

## **Time-line**

### **Starting Oct**

- Background reading on SED fitting of galaxies, star formation history and evolution in galaxies, stellar populations, colour-colour approach.
- Begin writing introductory chapter.

- Research data format etc. for MUSE, HST, GALEX, SDSS data.  $\lambda$  range, PSF, photo-calibration.
  - Understand how to calibrate the MUSE, GALEX, HST and SDSS data.
  - Provide example of calibrated SEDs for various regions of NGC7742 (e.g nucleus, ring, etc)
- Begin writing data chapter.

### **Starting Dec**

- Poster presentation (1 Dec). Featuring: Background, proposed methodology, example of calibrated spectro-photometric SEDs for NGC7742, and preliminary results from Summer.
  - Introduction, data (photometry), previous work from Summer.
- Testing.
- Have plan for layout / structure of report.
- Apply code for MUSE w/GALEX and MUSE w/HST data.

### **Starting Feb**

- Sample chapter and contents page (3 Feb)
  - Probably introductory chapter if not, data chapter may be quicker to write.
- Start writing application chapter.
- Student talk (16 Mar)
  - Hopefully have results of applying to real data by now. If not, can go into more detail on SED fitting etc. Hopefully include results of testing and applications.

**Starting Apr**

- Finishing, editing report.
- Report (21 Apr).
- Write viva presentation.
- Viva (11 May).

**II.2 Changes to the plan**

Due to time constraints, it was necessary to abandon the section on testing with synthetic star formation histories. I felt that conducting error analysis was more important. The introductory chapter was expanded to include concepts of attenuation and line of sight velocity distributions. This helped give context later on in the report, where the method and function of the SED fitting code was described. Some sections were moved to other chapters so that the layout was more logical.

# 1 Introduction

Reconstructing star-formation history is a crucial tool for understanding the evolution of galaxies. Astronomers are able to infer the star-formation properties of galaxies from multi-wavelength observations. This is because of the fact that the integrated light emitted from a galaxy is imprinted with the star formation history of that galaxy in terms of its principal stellar components. This star-formation history can generally be recovered by fitting to the spectral energy distribution (SED) of a galaxy. By finding the optimal fit of a library of stellar templates to a galactic SED, the associated weights for each template and thus the principal stellar populations can be found. Astronomers have typically relied on continuous optical spectra or on more spectrally comprehensive but sparsely sampled discreet broad-band photometric measurements to constrain star-formation history. There have been few attempts to combine both kinds of data (Chilingarian and Katkov, 2011). In this report a spectro-photometric to SED fitting is considered. This approach makes use of optical spectra with UV photometry, combining the advantages of highly detailed optical spectra with the comprehensive wavelength coverage possible with broad-band photometry.

The test case for this method is the ring galaxy NGC 7742. Using data from the MUSE integral spectrograph (Bacon et al., 2010) in combination with near and far UV data from the GALEX (Martin et al., 2005) and HST space telescopes it is possible to probe star-formation history across the spatial extent of the galaxy. The high-resolution MUSE spectrum combined with the extra information contained within the UV photometry makes it possible to constrain a more accurate star-formation history for this object.

The initial chapter of this report provides background on methods of recovering star-formation histories, particularly photometric and spectral SED fitting. It also introduces the test case, NGC 7742. §2 describes the data used including MUSE, SDSS, GALEX and HST. Methods for extracting the flux from different apertures and their corresponding errors are discussed. §3 details approaches to recovering star formation history using spectral data only and photometric data only. The limitations of each method are discussed. §4 details the combined spectro-photometric method that has been developed. §5 concerns obtaining uncertainties on the spectro-photometric fits. Errors are obtained by perturbing parameter values.

## 1.1 Background and early approaches

Baade (1944) was one of the first to consider the resolved stellar populations of galaxies. Taking advantage of blackout conditions enforced during the Second World War, Baade

was able to resolve the dwarf galaxies NCG 147 and NGC 185, satellites of M31, into their individual stars. Baade noted the differences between the ages of the stellar populations that he saw in the dwarf galaxies and in the Milky Way. Stellar populations in galaxies were separated into two distinct populations: young, Population I stars and older, Population II stars. This discovery helped make clear the possibility that star formation histories may be accurately derived from the resolved stellar populations of galaxies.

One of the earliest attempt to quantify star formation history (SFH) was by Searle et al. (1973) who were able to determine how the colour of light from galaxies was reflected in their star formation history. Various other indicators of star formation rate have been found, such as H- $\alpha$  emission line flux, infrared and UV luminosity and emission line ratios (Calzetti, 2013). Colour-magnitude and colour-colour diagrams made it possible to obtain more detailed star formation histories (Tolstoy et al., 2009; Peletier, 2013).

An approach which will be explored later in §1.4 is SED fitting with stellar synthesis models. This method allows us to recover the principal stellar components of a galaxy by fitting a number of stellar templates to a galaxy's observed SED. Early approaches using photometric and low resolution spectro-photometric observations were promising but inconclusive due to more limited early models (Schiavon, 2010).

Initial attempts relied on trial and error. Population synthesis models consisted of individual stellar spectra, which were added linearly in an attempt to build an astrophysically plausible reproduction of the observed integrated spectrum of a galaxy. See, for example, the method employed by O'connell (1976). Stellar spectra were taken from comprehensive libraries of stars of different type, age and mass (Bruzual and Charlot, 2003b). This approach has the advantage that there is no need to consider the evolution of stellar populations, for which there are large systematic uncertainties especially for highly evolved stars such as red giants and AGB stars. This is because there is still a poor understanding of these later stages of stellar evolution (Leitherer, 2004; Bruzual and Charlot, 2003b). However, this technique proved untenable in many cases due to the large number of free parameters involved, which make the model excessively complex. The typical galactic SED is not well sampled enough to cope with so many parameters, and this often results in over fitting, resulting in unphysical fits to the SED and making it impossible to constrain the true distribution of stars in age, mass, type, metallicity etc.

More recent models are based on models of stellar evolution and are known as evolutionary population synthesis models (Bruzual and Charlot, 2003b). With evolutionary population synthesis models, after an initial mass function and star formation rate have been set, the distribution of stars and therefore, the intrinsic integrated spectrum of

a galaxy, is only dependent on their age and metallicity. This results in a more astrophysically correct model which has fewer free parameters and is therefore easier to fit.

## 1.2 Stellar population synthesis

Very crudely, a galaxy is made up of populations of stars, each distributed in age, metallicity and mass. Each star in the galaxy contributes to the galaxies integrated light so that the spectral energy distribution of light emitted by a galaxy can be represented by the sum of the SEDs of each star that comprises it. This method of constructing a model spectrum is called stellar population synthesis.

In practice, the SED of a galaxy is modeled through the superposition of the spectra of a number of simple stellar populations (SSPs).

### 1.2.1 SSPs

A simple stellar population, or SSP, is an idealised collection of stars formed at the same time and from the same material (Walcher et al., 2010). This is analogous to a star cluster, whose stars are formed from a common molecular cloud. Because of this, the stars within an SSP have the same age and metallicity. The distribution of masses for stars within the cluster is dependent on an initial mass function (IMF) and models of stellar evolution. The combined spectrum of an SSP is just the sum of the spectra of the individual stars that comprise it (Walcher et al., 2010):

$$S_\lambda(t, Z) = \int_{m_l}^{m_u} \phi(m)_{t,Z} S_\lambda(m, t, Z) dm \quad (1.1)$$

Here,  $S_\lambda(t, Z)$  is the spectrum of the SSP in units of Flux per unit wavelength per unit mass.  $S_\lambda(m, t, Z)$  is the spectrum of a star with mass  $m$ , age  $t$  and metallicity  $Z$  and  $\phi(m)_{t,Z}$  is the stellar mass function.  $\phi(m)_{t,Z}$  is calculated from the IMF,  $\phi_0(m)$  and stellar evolution models.

The IMF is the expected distribution of masses that stars will have upon birth, essentially it gives the probability that a star will be born with a mass of  $m$ . So an SSP with an age of zero will have a spectrum that is simply the IMF at each step,  $\phi_0(m_i)$  multiplied by the corresponding stellar spectrum,  $S_\lambda(m_i, Z)$  and summed over the mass range. The IMF has many forms, but is usually given as a power law or broken power law of the form

$$\xi(m) \Delta m = km^{-\alpha} \quad (1.2)$$

so that  $\xi(m) \Delta m$  specifies the number of stars born with a mass in the range  $[m, m + dm]$ . Where  $k$  is a constant of the local stellar density and the index  $\alpha$  is 2.35 in the case of the Salpeter IMF (Krumholz, 2011). Since the index is negative, we can see that far more low mass stars are formed than high mass stars.

There is a further subtlety determining the SED of a simple stellar population because  $\phi_0(m)$  only describes the distribution of stars immediately after they have been formed. To properly determine the SED, we also need to consider stellar evolution (Walcher et al., 2010). Over the course of their lifetime, the spectral properties of stars will change dramatically. Stars more massive than  $8M_\odot$  will end their lives in supernovae, their cores collapsing to form a black hole or neutron star. Intermediate mass stars of  $m < 0.5M_\odot$  will evolve along the red giant branch and once their core becomes massive enough for Helium fusion, they evolve onto the asymptotic giant branch. When all of their fuel is expended they will end their life by contracting, expelling their outer layers in the process. Left behind is a planetary nebula with a white dwarf at its centre. In the absence of any more fuel, the white dwarf gradually radiates its residual thermal energy, cooling and becoming increasingly faint as it does so. Low mass stars will eventually become red giants but will never reach the tip of the red giant branch as their cores will not become massive enough to allow Helium fusion. Once their fuel has been expended, they too become white dwarfs.

As stars evolve along their evolutionary tracks, their SED and thus their contribution to the SED of the SSP as a whole changes and in the case of high mass stars, they may entirely cease to contribute. Stellar evolution models tell us about the spectral evolution of an SSP i.e. how SEDs of its constituent stars change over time.

Usually, the spectral energy distribution of each SSP is normalised by mass, so that they correspond to the same initial mass in stars (i.e. the mass at  $t = 0$ ).

### 1.3 Spectroscopic and photometric studies

Astronomical spectrographs generally consist of a slit through which light is focused, a collimator and a grating, which diffracts light into its component wavelengths, producing a continuous distribution of fluxes as a function of wavelength (Massey and Hanson, 2013). This spectrum is then focused through a lens onto a detector, allowing the intensity of light to be placed into wavelength bins whose size is dependent on the resolution of the grating and the detector. Spatially resolved spectroscopy of an extended source such as a galaxy can be achieved using a long slit placed over the object. This produces a one-dimensional, spatially resolved spectrum across the object. By rotating or moving the slit across the object, a spectrum can be built up in two spatial dimensions. The resulting data cube consists of two spatial dimensions and one wavelength dimension:

a spatially resolved spectral image where each pixel has a spectrum.

In reality, it is rarely practical to obtain a complete data cube in this way, as it would be very costly in terms of telescope time to move the slit after each exposure. Integral field spectroscopy is a technique that allows the entire data cube to be captured in a single exposure. Often this is achieved using an image slicer, which separates the incident light into a series of equal slices (Massey and Hanson, 2013). Spectroscopy allows for detailed study of the light from an object including its spectral lines. However, the cost of this precise spectral information is the long integration time required for a usable signal to noise ratio. Additionally, spectra tend to have relatively limited wavelength coverage.

Photometry utilises filters sensitive to light over a finite bandpass. By using multiple filters a spectral energy distribution can be constructed from a series of average fluxes within discrete wavelength intervals. The main advantage of this approach is the much shorter integration time required, particularly for broad-band filters. Since a single filter samples a large range of wavelengths, the flux of photons per bin is much greater than is the case for spectroscopy making broad-band photometry much cheaper in terms of telescope time required. Photometry is available over a wide range of wavelengths; this allows the construction of poorly sampled SEDs with large wavelength coverage.

Optical spectra and photometric images can be easily obtained by Earth based observatories, but ultraviolet and infrared wavelengths are readily absorbed by the atmosphere, making UV and IR astronomy possible only in the upper atmosphere and from space. Currently, many space telescopes are better equipped for photometry than spectroscopy, making photometry more widely available at a wider range of wavelengths than spectroscopy.

## 1.4 Reconstructing star formation history

In order to reconstruct the star formation history of a galaxy, we need to combine the ideas of simple stellar populations, attenuation due to dust and stellar kinematics. We view the galaxy as a super-position of simple stellar populations, the light from which has been attenuated by dust and the spectrum broadened by the dispersion in the average movement of stars. By using SED fitting, the principal stellar components can be identified and the star formation history thus recovered.

### 1.4.1 SED fitting

An SED is defined as a series of wavelengths with associated fluxes, these can be spectroscopic, photometric or a combination of both. SED fitting codes fit the observed SED of a galaxy to a grid of synthetic SSPs or stellar templates, each being assigned

a weight during the fit. The stellar templates consist of a library of SEDs for SSPs across a range of ages and metallicities and with the same initial total mass (Peletier, 2013; Schiavon, 2010). These templates must first be treated according to the dust attenuation and stellar kinematics of the galaxy. Emission nebulae must also be accounted for, either by masking emission regions or by including models for ionised gas emission in the fit.

An SED fitting code tries to find the best fit for the stellar composition of the galaxy and thus the ages and metallicities of the simple stellar populations that comprise it. This makes SED fitting an essential tool for recovering the history of star formation in galaxies.

Reconstructing the star formation history of a galaxy is a problem of inversion (Walcher et al., 2010). Obviously, we cannot derive the star formation history directly, instead we must find the input parameters to the model, which best reproduce some observational data that we have. In general, we solve inversion problems by minimising a cost function such as

$$\chi^2 = \sum_{i=0}^n \left[ \frac{(O_i - E_i)}{\sigma_i} \right]^2 \quad (1.3)$$

Where  $O_i$  is an observed data point,  $E_i$  is the corresponding data point predicted by the model for some set of input parameters and  $\sigma_i$  is the corresponding error on the observed data. By finding the input parameters to our model which minimise the cost function and thus best fit the data, we are inferring properties of an object that are not obtainable directly from the data itself.

The SED of a galaxy can be represented by the weighted sum of the SEDs of individual SSPs (such as the SEDs shown in Figure 1.1), which have been treated for dust attenuation, stellar kinematics and emission nebula. In the case of the star formation history, given a number of template SSPs, the main parameters of interest are the weighting that we give to a grid of SSP templates. By finding the weights attributable to each SSP that best reproduce our observations of the galaxy, we can thus recover the star-formation history as a sum of  $\delta$  functions.

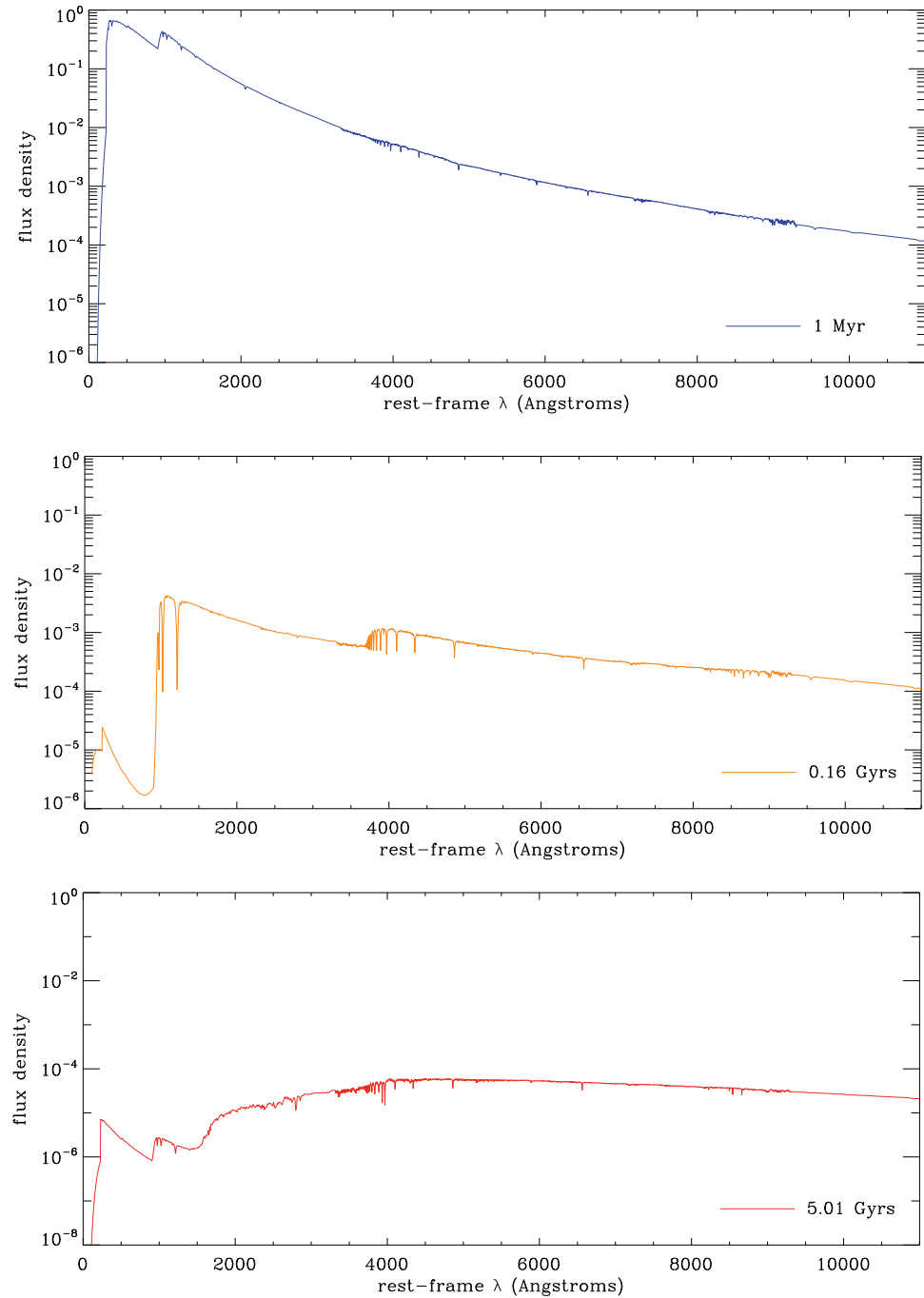


Figure 1.1: Example individual stellar templates for  $[\text{Fe}/\text{H}] = -1.6464$  with age 1 Myr, 0.16 Gyrs and 5.01 Gyrs. The intensity of the UV component decreases with age as more massive stars cease to contribute. Meanwhile, the visible and near IR components retain a similar shape and intensity as less massive stars continue to shine.

### 1.4.2 Reddening due to dust

Because stars are formed exclusively from molecular clouds, star forming galaxies are associated with large densities of molecular Hydrogen ( $H_2$ ).  $H_2$  clouds, in turn, imply the presence of dust because molecular Hydrogen is known to be formed when atomic Hydrogen (HI) is adsorbed onto the surface of dust grains. In addition, star formation itself is responsible for the production of dust because young, massive stars enrich the ISM with heavy elements and dust via supernovae and stellar winds (Leitherer, 2005).

The presence of dust and gas in star forming galaxies introduces uncertainty when trying to correctly interpret their galactic SED in terms of stellar population. It is necessary to quantify the effect that dust obscuration has had on incident starlight in order to recover the galactic SED as it would look in the absence of this dust obscuration. In doing this we can identify the total contribution to the SED by all stars and thus infer the stellar population.

Dust along the line of sight effects starlight in a number of ways:

1. By physically obscuring objects from view
2. By attenuating light through absorption and scattering away from the line of sight
3. By absorbing and re-emitting photons, transforming their energy from the optical to IR

Figure 1.2 illustrates these effects, showing the ways in which the energy, intensity and direction of starlight is changed on its journey to the observer.

The extinction of the light from a single star depends only on column density along the line of sight and the efficiency at which the dust grains absorb and scatter light out of the line of sight. The distribution of dust in the foreground is irrelevant to the extinction of a point source, so it is valid to assume that the dust between the star and the observer forms a screen of uniform extinction.

Distinct from point sources, an extended object instead suffers an attenuation of emitted light dependent on the distribution of dust and stars. Assuming a uniform screen between object and observer is no longer valid. The light from different stars will encounter different column densities of dust before reaching the observer, some stars embedded within dust clouds will suffer internal extinction, while others may find themselves in the foreground of the dust distribution of the observed galaxy and thus suffer no attenuation. Additionally, light may be scattered both into and out of the line of sight due to the more complex geometry that a distribution of stars and dust has. As a result, the effective attenuation of an extended object is generally less than the extinction expected for a single, point object (Calzetti, 2001, 2013).

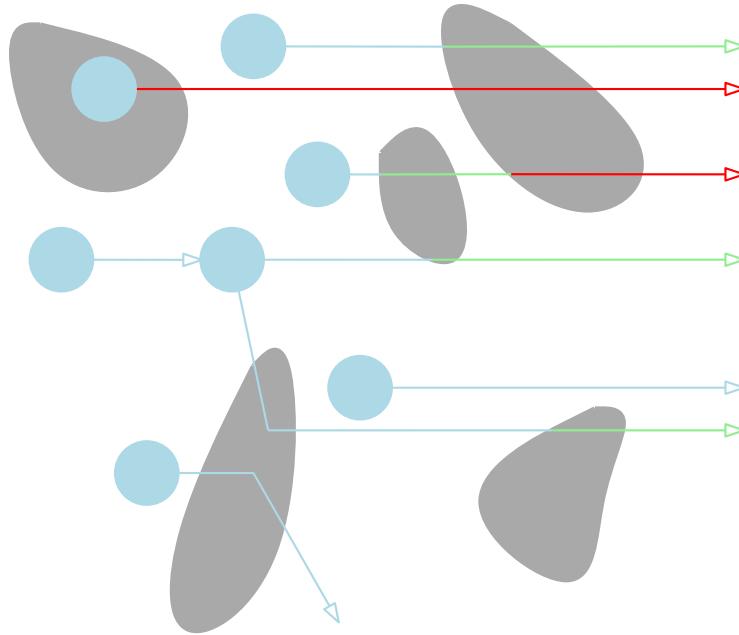


Figure 1.2: Starlight is attenuated differently depending on how it travels through dust clouds. A star might be foreground to the distribution of dust, in which case there is no attenuation or it might be embedded in a dust cloud so that its light is suffered internal attenuation. Light may be scattered into and out of the line of sight.

A common attenuation law for starburst galaxies is the Calzetti Dust Extinction Law, this is a piecewise power law given by Calzetti et al. (2000):

$$k(\lambda) = \begin{cases} 2.659 \left( -2.156 + \frac{1.509}{\lambda} - \frac{0.198}{\lambda^2} + \frac{0.011}{\lambda^3} \right) + R_V & 0.12\mu\text{m} \leq \lambda \leq 0.63\mu\text{m} \\ 2.659 \left( -1.857 + \frac{1.040}{\lambda} \right) + R_V & 0.63\mu\text{m} \leq \lambda \leq 2.20\mu\text{m} \end{cases} \quad (1.4)$$

where  $k(\lambda)$  is the reddening curve,  $\lambda$  is the wavelength in  $\mu\text{m}$  and  $R_V$  is the total-to-selective extinction ratio, which is equal to  $4.05 \pm 0.8$ .

The light attenuation of the starburst regions of local galaxies is best described by the model of a shell of clumpy dust around the region. This allows the star-dust geometry to be treated as a foreground screen with attenuation dependent on a single attenuation law applied to the spectrum of the galaxy as a whole (Calzetti et al., 1994). Since  $k(\lambda)$  is the ratio of total to selective attenuation of the stellar continuum light,  $k(\lambda) = A(\lambda)/E(B-V)_*$ , the intrinsic SED of an object whose attenuation is well approximated by this model is given by

$$S_{\lambda,int} = S_{\lambda,obs} \cdot 10^{-0.4(E(B-V)_*)k(\lambda)} \quad (1.5)$$

where  $S_{\lambda,obs}$  is the observed SED and  $E(B-V)_*$  is the selective attenuation (Calzetti et al., 2000; Fischera et al.; Calzetti et al., 1994).

The Calzetti Dust Extinction Law is derived purely empirically from large numbers of observations of starburst galaxies in different bandpasses.

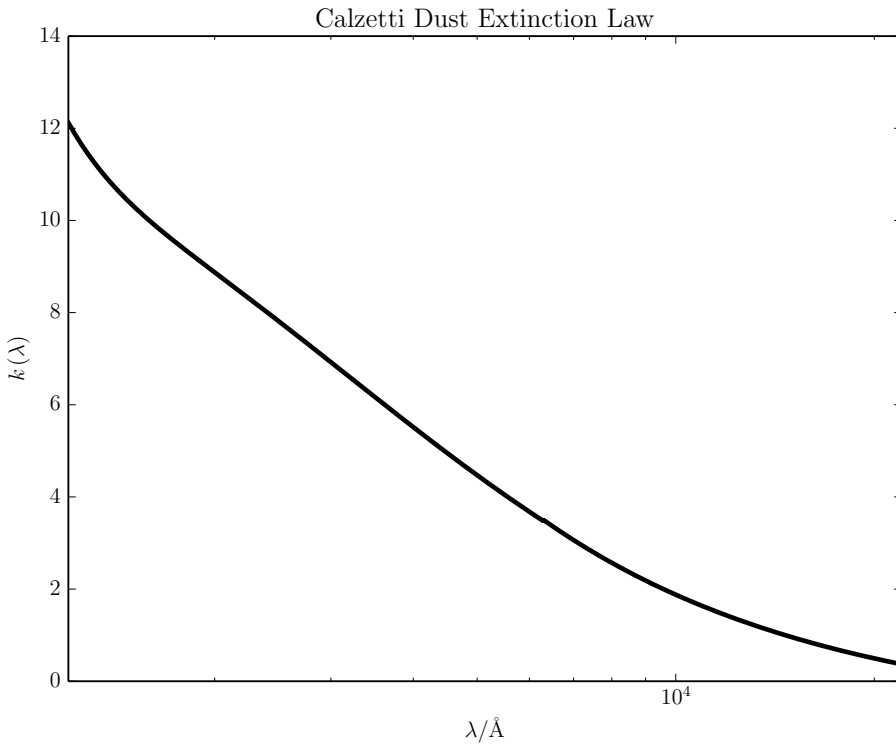


Figure 1.3: Extinction curve,  $k(\lambda)$ , for the Calzetti Dust Extinction Law

We can see from Figure 1.3 that light is more severely attenuated as its wavelength moves towards the ultraviolet, while redder light sees little attenuation. The result of this is reddening of the galactic SED. Since young, massive stars emit light primarily in the UV, they are most affected by attenuation due to dust. As a result treating the spectrum of a galaxy for dust attenuation is especially important when considering the young population.

Stars that are embedded in HII regions will suffer an additional attenuation due to internal reddening. HII regions, which are clouds of ionised gas where star formation has recently taken place, are created when young, massive stars, which are formed in molecular clouds are able ionise the surrounding hydrogen due to their UV luminosity. Still embedded in the dust they were formed from, the light from stars in young SSPs ( $\lesssim 10$  Myrs) suffers additional ‘birth cloud’ attenuation as they are further obscured by the their birth material (Walcher et al., 2010). When studying young stellar populations, it is necessary to account for this by adopting a model incorporating attenuation due to the diffuse ISM dust as well as the concentrated dust of the stellar birth cloud. As Figure 1.4 illustrates, the inclusion if additional reddening can have a profound effect on the SED, especially in higher energy domains.

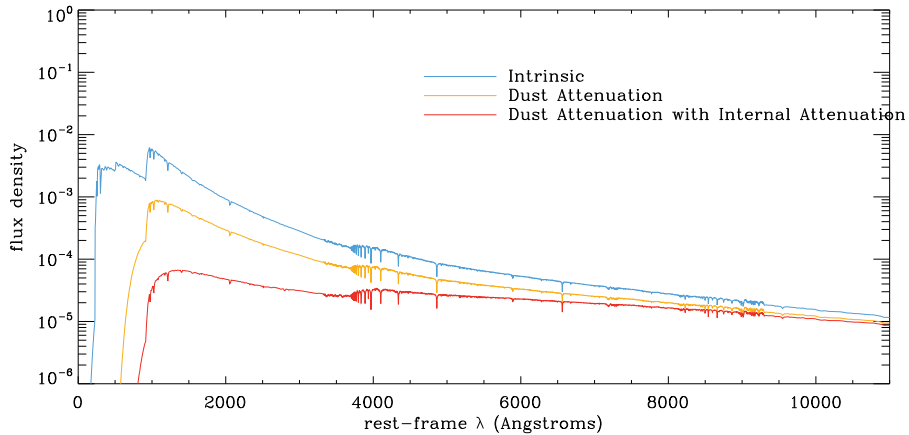


Figure 1.4: An intrinsic galactic SED created from a mixture of SSPs, attenuated and internally attenuated. We can see that the UV end of the spectrum is most effected by dust attenuation. Including attenuation for young templates further decreases the UV flux density but barely effects the flux density after  $\sim 8000\text{\AA}$  since the contribution by young templates becomes negligible.

#### 1.4.3 Stellar kinematics

The spectrum of a distribution of stars is the sum of the individual stellar spectra redshifted according to their line of sight velocities (Cappellari and Emsellem, 2004). The observed spectrum, then, is the convolution of the intrinsic, mean stellar spectrum and the line of sight velocity distribution (LOSVD). Early methods such as by those employed by Sargent et al. (1977) use Fourier techniques to deconvolve the LOSVD from the observed galactic SED. Today, the LOSVD is calculated directly in pixel space. A

model spectrum for the galaxy is created by convolving a template spectrum,  $S(x)$ , with a LOSVD,  $\mathcal{L}(v)$ , so that

$$S_\lambda = [\mathcal{L} \star S](x) + \sum_{n=0}^N b_n P_n(x). \quad (1.6)$$

which is solved for each  $\mathcal{L}(v)$ . Here,  $b_n$  are the weights associated with the Legendre polynomials,  $P_n(x)$ . These compensate for any low frequency variations between the model and galaxy spectrum (Cappellari and Emsellem, 2004). The LOSVD is determined by a Gauss-Hermite series:

$$\mathcal{L}(v) = \frac{\exp(-\frac{1}{2}y^2)}{\sigma\sqrt{2\pi}} \left[ 1 + \sum_{m=3}^M h_m H_m(y) \right] \quad (1.7)$$

where  $y = (v - v_{fit})/\sigma$ .  $\mathcal{L}(v)$  can be recovered by solving for velocity,  $v_{fit}$ , velocity dispersion,  $\sigma$ , and the Hermite coefficients  $h_3$  to  $h_M$ . This can be achieved by minimisation of a  $\chi^2$  cost function.

For more dynamically simple galaxies, like ellipticals, the LOSVD is close to Gaussian but the LOSVD can become more complex for complicated structures. Stellar kinematics have the effect of broadening spectral lines, so to obtain a correct fit to the data, it is necessary to derive a line of sight velocity distribution. The LOSVD is used to broaden and shift the model spectrum so that it is consistent with the data.

Figure 1.5 shows an example of a line of sight velocity distribution found from MUSE spectra of NGC 7742. While roughly Gaussian, the LOSVD also exhibits a partial second peak.

#### 1.4.4 Photometric and spectroscopic SED fitting

Once the stellar kinematics have been derived, it is possible to fit the galactic SED by minimising the following cost function:

$$\chi^2 = \sum_{i=0}^n \left[ \frac{(O_i - \sum_{j=1}^N a_k S_j [t_k, Z_k, E(B-V)_*])}{\sigma_i} \right]^2 \quad (1.8)$$

where  $O_i$  is  $i^{\text{th}}$  wavelength bin of the observed galactic spectrum, or the  $i^{\text{th}}$  band-pass bin of the observed photometric SED,  $\sigma_i$  is the corresponding standard deviation and  $\sum_{j=1}^N a_k S_j [t_k, Z_k, E(B-V)_*]$  is a synthetic spectrum made up of the sum of stellar templates  $S_j$  with age  $t_k$ , metallicity  $Z_k$ , and selective attenuation  $E(B-V)_*$  each

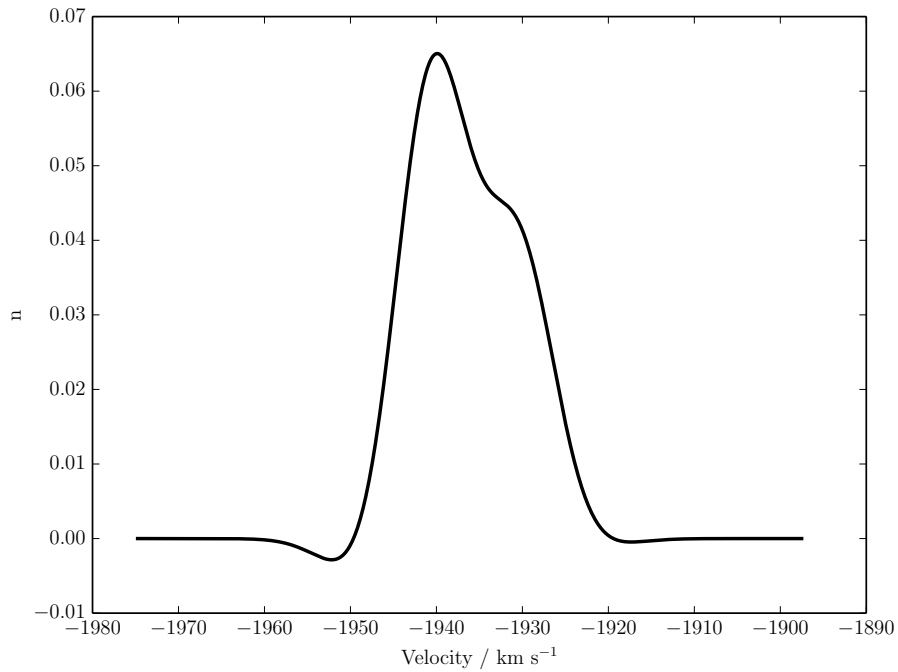


Figure 1.5: An example of a line of sight velocity distribution,  $\mathcal{L}(v)$ , derived from MUSE spectra for a portion of the disk of NGC 7742.

weighted by  $a_k$  (Walcher et al., 2010). As mentioned in §1.4.2, a screen approximation allows us to ignore the fact that, in reality, stellar populations reside at different optical depths. Therefore only a single  $E(B - V)$  parameter is fit. So essentially, the same attenuation is assumed for all templates.

In the case of a photometric SED, kinematics do not need to be considered because wide bandpasses mean that the effect of a broadened spectrum will be negligible. The lack of fine detail provided by broad-band photometry makes it unsuitable for many applications. SED fitting using photometric data is used mainly to gauge the age of stellar populations and to estimate photometric redshift measurements for large numbers of objects. For example see ?.

As a result of finer sampling, SED fitting with spectroscopic data is a more precise tool with a wider range of applications. These include deriving star formation history and quantifying attenuation and emission due to dust among others (Walcher et al., 2010).

## 1.5 Recovering star formation history with MUSE

MUSE is an integral field spectrograph installed on the VLT, it operates in the visible wavelength range from 4650Å and 9300Å (Bacon et al., 2010). When extrapolated into the UV, a fit using only the MUSE spectrum does not always accurately reflect the true UV flux density of a galaxy. It is possible that this is due to the fact that the UV component of the galactic spectrum contains information about young stars which is not present in the optical. If this is true, the addition of UV photometric fluxes to the fit will make it possible to constrain a more accurate star-formation history.

This project concerns developing and testing such a spectro-photometric approach to SED fitting. Changes were made to the GANDALF SED fitting code (Sarzi et al., 2006) in order to fit a combination of spectroscopic fluxes from MUSE as well as photometric UV fluxes from GALEX and the SDSS.

### 1.5.1 Test case: NGC 7742

The initial test case is NGC 7742, a face-on Sa galaxy which is host to a starburst ring about its nucleus. NGC 7742, therefore, contains a super-position of young and old stellar populations, making it an excellent test case for recovering star formation history. Integral field spectroscopy from MUSE makes it possible to probe star formation history across the spatial extent of the galaxy.

By separating the galaxy onto annuli for the bulge, ring and disk, and by summing up the spectra in the MUSE data cube falling within the annuli, it is possible to spatially probe the star-formation history of NGC 7742. The nuclear ring is a good test for the method, as it should contain a combination of old and young stars. This is the result of recent star formation in the ring, which was triggered by the acquisition of fresh material. When the MUSE data is combined with data from GALEX or HST photometry it should be possible to more accurately constrain this recent star formation in NGC 7742.

## 2 Data

For the test case galaxy, NGC 7742, photometric data from GALEX and SDSS along with integral field spectroscopy from MUSE was used.

### 2.1 MUSE

The Multi Unit Spectroscopic Explorer (MUSE), is a large format integral field spectrograph installed on the Very Large Telescope (VLT), utilising image-slicing technology

(Bacon et al., 2010; Richard and Bacon, 2015). It began operation in January, 2014. MUSE operates across almost the entire visible wavelength domain, from 4650Å to 9300Å and is able to achieve a median angular resolution of 0.4 arcseconds in wide field mode (WFM) (Richard and Bacon, 2015).

The 1 arcmin<sup>2</sup> MUSE field of view is split into 24 channels by the field splitter and each image slice is sent into one of 24 integral field units (IFUs). Each slice of the image is further split into 48 slices by the image slicer in each IFU, for a total of 1152 ‘mini-slits’. The image slicer also rearranges the two-dimensional image slice into a single long slit with a width of 0.2”. In addition to an image slicer, each IFU contains a spectrograph and detector. Light passes through the spectrograph, producing a spectra of the mini-slits which are then imaged onto a 4096 × 4112 pixel detector. Each of the spectra are sampled at a resolution of 1.25Å per pixel.

In WFM, MUSE samples a 1 arcmin<sup>2</sup> field of view at 0.2” per pixel. In the future, MUSE will begin operating in narrow field mode (NFM). By utilising the VLT’s adaptive optics facilities, MUSE will be able to cover a 7.5 arcsec<sup>2</sup> field of view sampled at a resolution 0.025” per pixel and at an angular resolution of ∼ 0.05” (Richard and Bacon, 2015).

Observations by MUSE are stored as a datacube in FITS format. This is a three dimensional array with two spatial RA and DEC axes and one wavelength axis. This can be thought of as an array of two-dimensional images as a function of wavelength or as a two dimensional array of spectra as a function of position. Measurements are in terms of flux density in erg s<sup>-1</sup> m<sup>-2</sup> Å<sup>-1</sup>. Figure 2.1 shows one of the ways in which the datacube can be decomposed. It shows four slices in succession, extracted from the MUSE datacube. One can also imagine how the spectrum would look at any point in the galaxy by examining how the intensity changes between slices.

### 2.1.1 Errors

A second datacube gives the MUSE errors. Just like the MUSE data, the error datacube has two spatial dimensions plus a dimension of wavelength. These errors are given as a variance,  $\sigma^2$ . Because errors are combined by adding in quadrature, the combined error in a region of the MUSE datacube can be found by simply taking the square root of the sum of the variances.

## 2.2 GALEX

The Galaxy Evolution Explorer (GALEX) is an orbiting telescope able to observe galaxies at ultraviolet wavelengths. Launched in 2003, GALEX operated for almost 9 years until it was placed into standby mode in 2012 and finally decommissioned in 2013

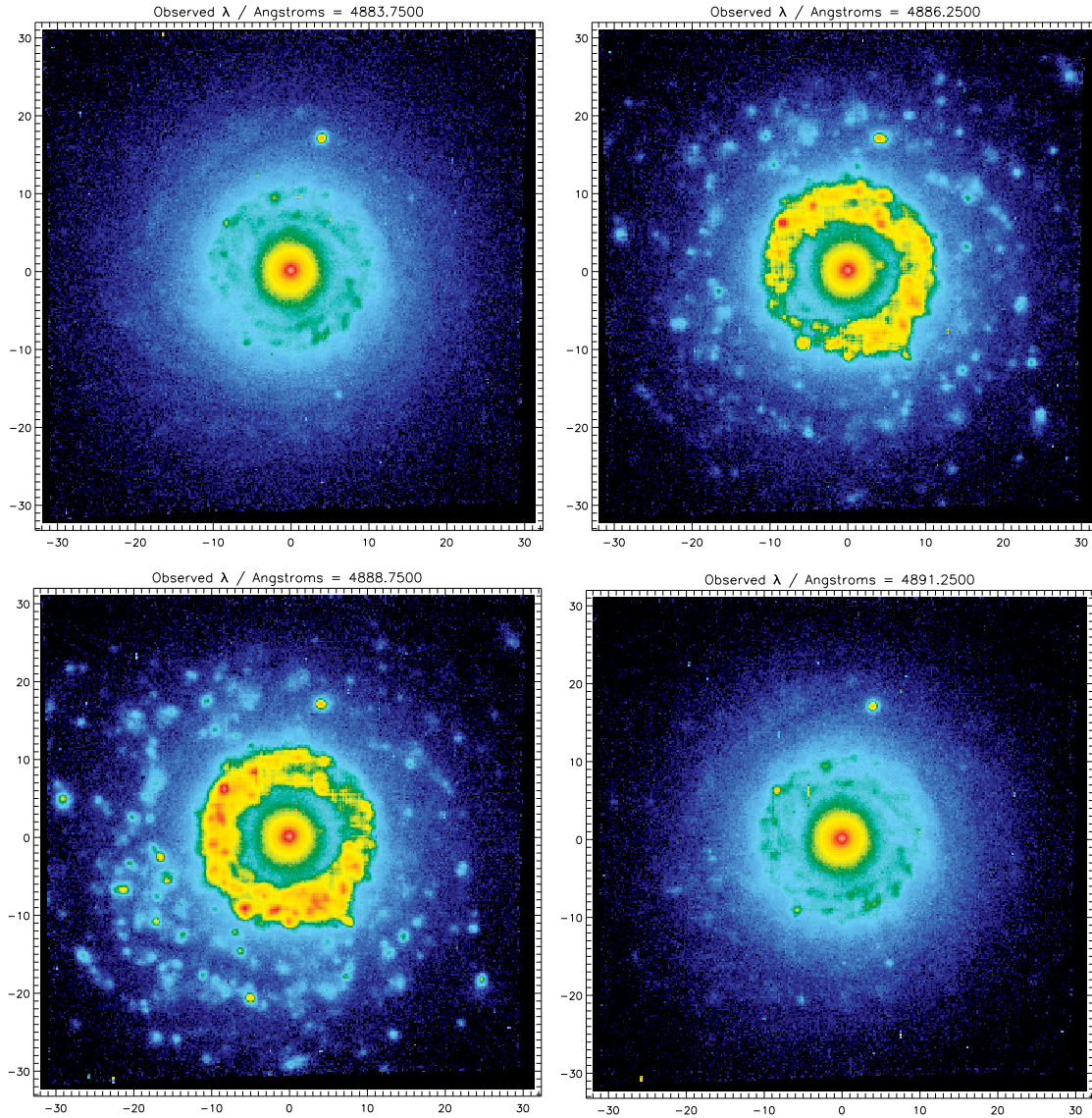


Figure 2.1: Images of NGC 7742 extracted from the MUSE datacube. 4 slices were extracted showing wavelengths close to the apparent wavelength of the H- $\beta$  spectral line. The central wavelength of the H- $\beta$  spectral line is 4861 $\text{\AA}$ . This corresponds to an observed wavelength of 4888 $\text{\AA}$ . We observe that different regions of the galaxy change in intensity by different amounts with wavelength. For example, we see bumps in the ring as a result of the H- $\beta$  line being blueshifted or redshifted as a result of the movement of gas. We also see larger scale changes such as the differences in intensity between the bulge and the ring.

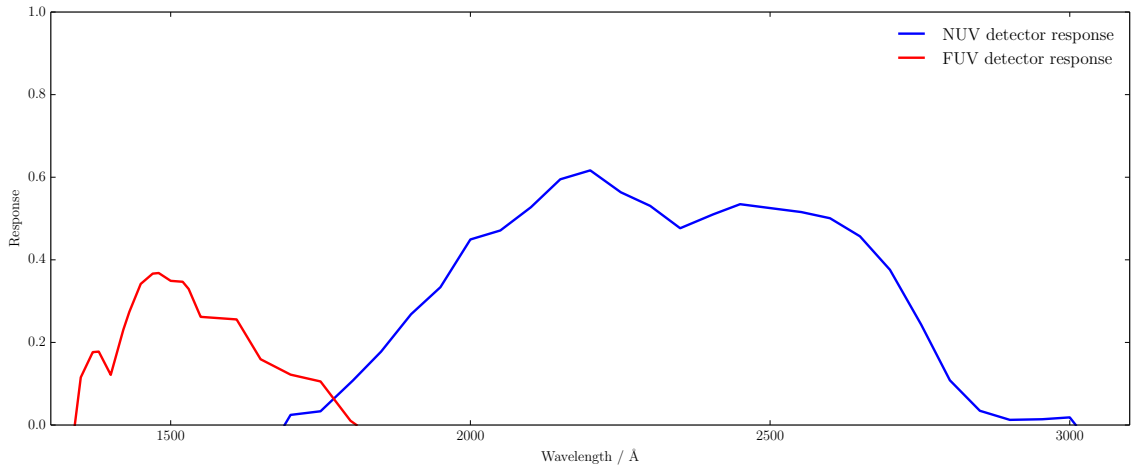


Figure 2.2: Response curves for the GALEX NUV and FUV detectors. The barycentric wavelengths of the NUV and FUV detectors are 2316Å and 1539Å respectively.

(Bianchi, 2014). A single GALEX tile covers a 1.2 degree diameter circular area of the sky. For all observations, light is passed through a beam-splitter and is subsequently recorded by far ultraviolet (FUV) and near ultraviolet (NUV) micro-channel plate detectors which reconstruct an image sampled at 1.5" per pixel. The FUV and NUV detectors have bandpasses ranging from 1340Å to 1805Å and 1693Å to 3007Å respectively, covering low to intermediate UV energies. Figure 2.2 shows the response curves for the two detectors.

With only a 50cm diameter primary mirror, GALEX achieves a resolution of 5.3" FWHM in the NUV and a resolution of 4.2" FWHM in the FUV (although GALEX is not, in fact, diffraction limited) (Morrissey et al., 2007). At a distance of 24Mpc (the distance to NGC7742), this corresponds to a spatial resolution of approximately 500 to 600 parsecs.

To extract fluxes from the GALEX image tiles, 'intbgsub' image tiles were downloaded. These tiles are available from MAST, the Mikulski Archive for Space Telescopes as .fits files. The 'intbgsub' tile is created by first dividing the raw intensity map, in photons per 1.5" pixel, by a relative response map, which is the sensitivity multiplied by the exposure time. Finally, the estimated sky background is subtracted to give an image in units of photons per pixel per second. This photon count rate can be converted to a flux density in units of  $\text{erg s}^{-1} \text{cm}^{-2} \text{\AA}^{-1}$  by multiplying by a conversion factor. These differ between the FUV and NUV:  $1.40 \times 10^{-15} \times \text{total counts per second}$  and  $2.06 \times 10^{-16} \times \text{total counts per second}$  respectively (Morrissey et al., 2007).

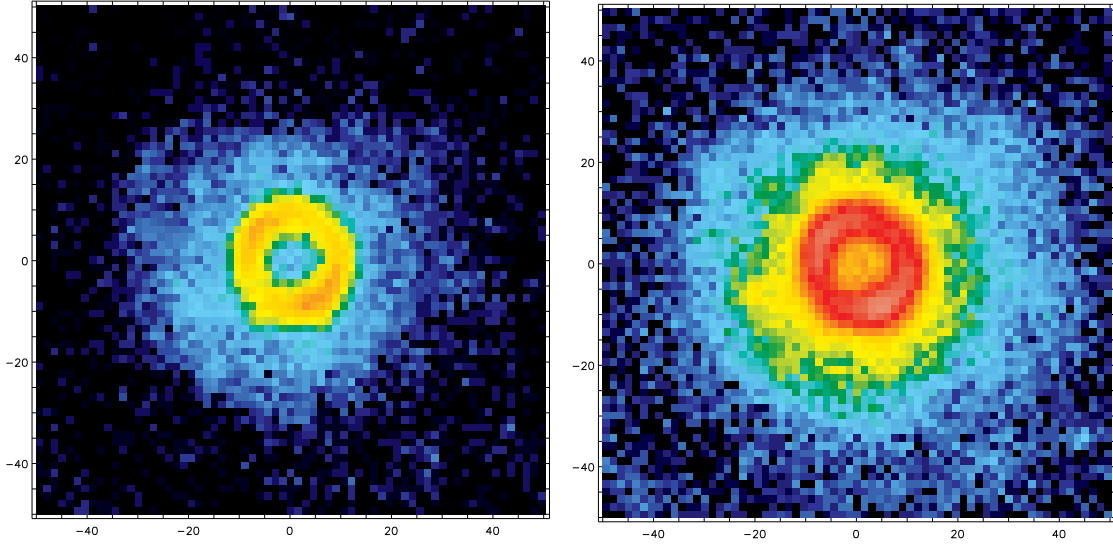


Figure 2.3: GALEX FUV and NUV images of NGC7742 with the same colour scale. GALEX tiles have a physical resolution of  $1.5''$  per pixel for both the FUV and the NUV detector.

### 2.2.1 Errors

Errors are assigned to the photometric flux for each detector and for each aperture in the same way as the error on the total flux is calculated in the GALEX MAST archive. Aperture photometry for objects in GALEX tiles is handled by SExtractor (?). The error in the number of counts,  $\delta f$ , as calculated by SExtractor and which is quoted in the MAST archive is given by

$$\delta f = \frac{\sqrt{(c + s\Omega)t}}{t} \quad (2.1)$$

where  $c$  is the flux within the aperture in photon counts per second,  $s$  is the sky background level in photon counts per pixel,  $\Omega$  is the area of the aperture in pixels and  $t$  is the exposure time. A separate NUV and FUV sky level can be found in the PhotoObjAll table in MAST under the `nuv_skybg` and `fuv_skybg` fields, the exposure time is found in the FITS image tile under the field `exptime`.  $\Omega$  is simply the number of pixels in an aperture and  $f$  is found by summing the values of each of these pixels.  $\delta f$  is given in photon counts per second.

Once we have the error on the number of photon counts, the error on the flux can be calculated. Counts are first converted to AB flux using:

$$m_{AB} = -2.5 \times \log_{10} (f) + m_0 \quad (2.2)$$

where  $m_0$  is the zero point corresponding to the AB magnitude of a 1 count per second source. There are zero points for the FUV and NUV detector are given by Morrissey et al. (2007) and are said to be accurate to  $\pm 10\%$ :

$$m_{0,\text{FUV}} = 18.82 \quad (2.3)$$

$$m_{0,\text{NUV}} = 20.08 \quad (2.4)$$

Once the zero points have been used to find the AB magnitude, the definition of the AB magnitude can be used to find the flux. AB magnitudes are scaled so that they have a zero-point of 3631Jy, so

$$m_{AB} = -2.5 \log_{10} \left( \frac{f_\nu}{3631\text{Jy}} \right) \quad (2.5)$$

where  $f_\nu$  is the flux density in terms of Jy. For  $f_\nu$  in cgs units of  $\text{erg s}^{-1} \text{cm}^{-2} \text{Hz}^{-1}$ , we instead get

$$m_{AB} = -2.5 \log_{10} (f_\nu) - 48.60 \quad (2.6)$$

which can then be inverted to find  $f_\nu$ , so that

$$\delta f_\nu = 10^{-0.4m_{AB}} 3631 \times 10^{-23} \quad (2.7)$$

Finally the error,  $\delta f_\nu$ , in terms of  $\text{erg s}^{-1} \text{cm}^{-2} \text{Hz}^{-1}$  is converted to  $f_\lambda$  in terms of  $\text{erg s}^{-1} \text{cm}^{-2} \text{A}^{-1}$  using the fact that  $\lambda f_\lambda = \nu f_\nu$

$$f_\lambda = f_\nu \frac{c}{\lambda^2} \quad (2.8)$$

where  $\lambda$  is in Å.

### 2.3 SDSS

The Sloan Digital Sky Survey (SDSS) is a multi-wavelength photometric and spectroscopic survey employing a wide-angle 2.5m telescope with a 3 degree field of view (Eisenstein et al., 2011). The SDSS 2.5m telescope's camera consists of an array of 30  $2048 \times 2048$  CCDs utilising a system of 5 filters: ultraviolet (u), green (g), red, (r), near infrared, (i), infrared (z). The CCDs are arranged in 5 rows of 6 CCDs with the u, g, r, i and z filters each covering one row. An image is built up simultaneously in each filter using the drift scanning technique. This technique sees the telescope utilising the Earth's rotation to scan across the sky, the telescope moves so that its field of view tracks great circles across the sky, keeping objects moving along the same column of pixels. The CCDs are continuously read out so that an image is built in strips of six parallel scan lines (Gunn et al., 1998). Figure 4.4 shows a schematic view of the SDSS camera, illustrating its movement with respect to the sky.

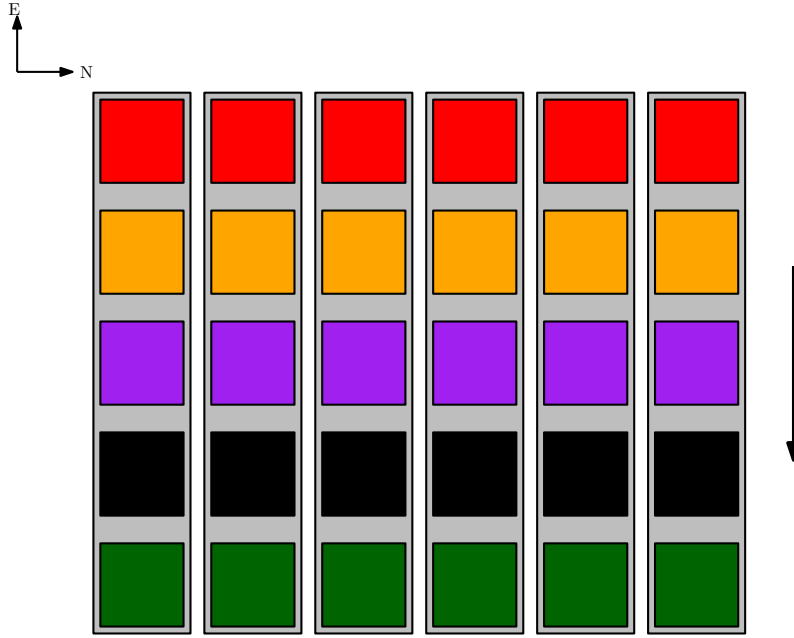


Figure 2.4: Layout of the SDSS camera. Filters are ordered  $r$ ,  $i$ ,  $u$ ,  $z$  and  $g$  from the top of the camera to the bottom. The arrow denotes the movement of the sky across the camera as the telescope tracks great circles across the sky.

The SDSS  $u$ ,  $g$ ,  $r$ ,  $i$  and  $z$  filters have ranges from 3048Å to 4028Å, 3783Å to 5539Å, 5415Å to 6989Å, 6689Å to 8389Å and 7960Å to 10833Å respectively. This gives SDSS a spectral range spanning the optical and parts of the infrared and ultraviolet. Response curves for the SDSS filters are shown in Figure 2.5 and images in each filter are shown in figure 2.6.

The SDSS telescope is ground based, so its angular resolution is limited by seeing. In ideal conditions, astronomical seeing can give an angular resolution 0.5" but the median angular resolution achieved by SDSS is around 1.5". The ideal angular resolution of 0.5" corresponds to a physical resolution of 60pc at 24Mpc (the distance to NGC 7742) (Eisenstein et al., 2011).

FITS files containing SDSS image fields for each filter are available to download from SDSS science archive server. A single SDSS field corresponds to one of the six scan lines for one of the 5 filters belonging to the SDSS 2.5m telescope's camera. Each field is an intensity map in units on nanomaggies per pixel measuring 10" by 13" and  $2048 \times 1489$  pixels. A maggy corresponds to approximatley 3631Jy, the AB magnitude zero-point. However, there are very small discrepancies between the SDSS and AB zero-points in

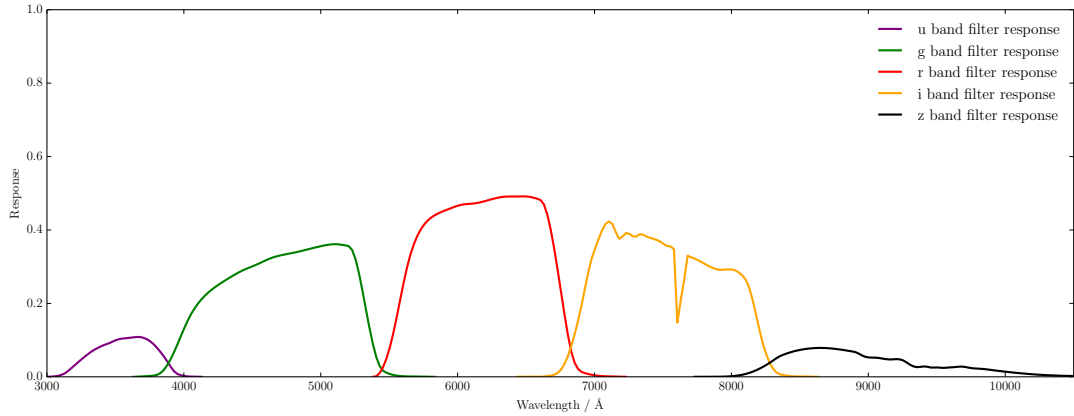


Figure 2.5: Response curves for the SDSS u, g, r, i and z filters. The barycentric wavelengths of the filters are 3562Å, 4719Å, 6185Å, 7500Å and 8962 Å respectively.

some filters. In order to convert nanomaggies to units of  $\text{erg s}^{-1} \text{cm}^{-2} \text{\AA}^{-1}$ , we must first convert to units of  $\text{erg s}^{-1} \text{cm}^{-2} \text{Hz}^{-1}$  and then convert to  $F_\lambda$  using the barycentric wavelength of the filter,  $\lambda_{\text{mean}}$ . The flux density in  $\text{erg s}^{-1} \text{cm}^{-2} \text{Hz}^{-1}$  will be

$$F_\nu [\text{erg s}^{-1} \text{cm}^{-2} \text{Hz}^{-1}] = F_\nu [\text{nanomaggies}] \times 3.631 \times 10^{-26} \quad (2.9)$$

because 1Jy is equal to  $10^{-23} \text{ erg s}^{-1} \text{cm}^{-2} \text{Hz}^{-1}$ . It is then simple to convert to  $F_\lambda$  as we did before for GALEX

$$F_\lambda [\text{erg s}^{-1} \text{cm}^{-2} \text{A}^{-1}] = \frac{F_\nu [\text{nanomaggies}] \times 3.631 \times 10^{-26}}{\lambda_{\text{mean}}^2/c} \quad (2.10)$$

### 2.3.1 Errors

The errors that are assigned to the photometric flux for each bandpass are calculated in the same way as the SDSS science archive server values. The photometric flux calibration page of SDSS data release site gives a formula for computing the error in terms of the image counts (nanomaggies)

$$\delta f = \sqrt{\frac{(f + \text{sky})}{\text{gain}}} + \text{Npix} (\text{DarkVariance} + \text{SkyErr}) \quad (2.11)$$

this gives the error in terms of counts per second. Here,  $f$  is the flux in the aperture in nanomaggies, the sky parameter gives the average sky level in the frame in terms of

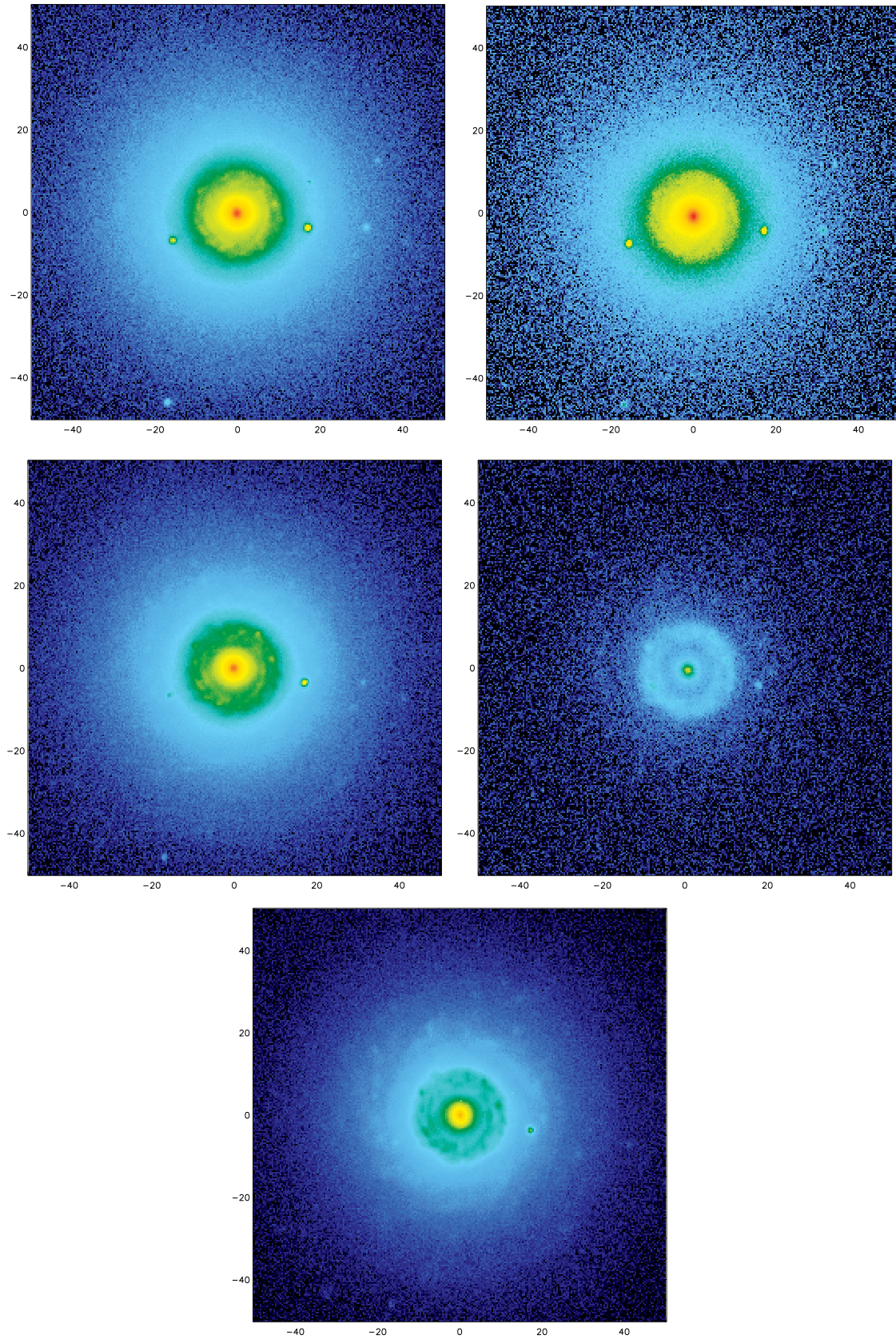


Figure 2.6: SDSS u, g, r, i and z images of NGC7742 with apertures with the same colour scale.

nanomagies per pixel for each filter, the gain parameter gives the average gain used for each filter over the exposure, DarkVariance is the variance of the dark current and SkyErr is the error for the estimate of the average sky level for each filter. The gain, darkvariance and skyerr values are all found in the field table for the data release.

## 2.4 Combined data

Figure 2.7 shows the wavelength coverage of the masked spectrum as well as the filter bandpasses. We can see that the combined GALEX and SDSS photometry with MUSE spectra are able to cover almost the entire wavelength range from far ultraviolet to infrared in varying degrees of detail. Although they have not been used in this project, Hubble space telescope data is also available for NGC 7742 in the f336w, f565w, f657w and f814w filters. The spectrum for NGC 7742 is not well flux calibrated for the whole wavelength range of MUSE, so significant portions have been masked out. The spectrum however, still contains features important for the fitting process such as the H- $\alpha$  and H- $\beta$  spectral lines, which are important for calculating the extinction through the Balmer decrement.

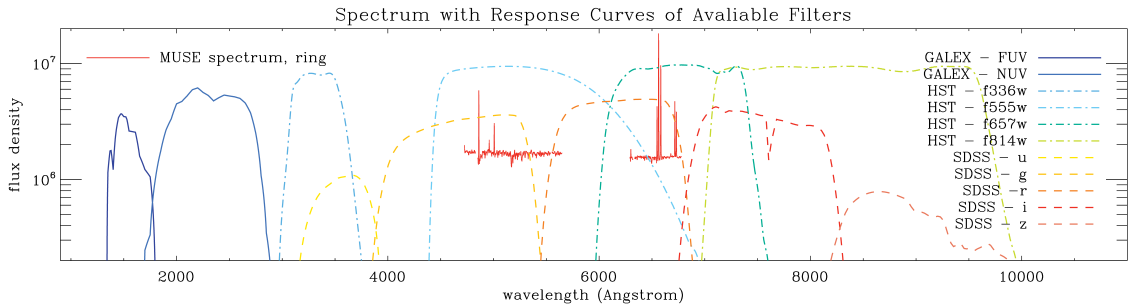


Figure 2.7: Response curves for GALEX, SDSS and HST filters with the masked MUSE spectrum for NGC 7742.

## 2.5 Templates

In order to be suitable for our purposes, the template library used in the fitting process needs to cover an appropriate wavelength range and make use of spectra for a wide range of spectral types, including for hot stars, since we are interested in regions with ongoing star formation. To break the age-metallicity degeneracy, it is necessary to be able to compare the relative strengths of different stellar absorption line features (Bruzual and Charlot, 2003b). These stellar absorption spectral indices, which exist

mainly in the optical and near infrared, must be well sampled by both the observed and template spectra. Since the spectral indices of the observed spectrum and the data are compared, it is necessary to be able to predict the actual observed spectrum of the galaxy at the same spectral resolution as the data.

A template library suitable for this purpose is GALEXEV (Bruzual and Charlot, 2003b,a). Also known as BC03, GALEXEV is a library of stellar population synthesis models covering a variety of metallicities and ages. The Bruzual and Charlot (2003b) model is able compute the spectral evolution of an SSP for ages between 10,000 yrs and 20 Gyrs in 221 time-steps and across a wavelength range between 91Å and  $1.6 \times 10^6$ Å at various spectral resolutions. GALEXEV has a spectral resolution of  $\lesssim 3$ Å FWHM for the entire range from the near infrared to the optical (3200Å to 9500Å) (Le Borgne et al., 2003) which is a range containing important spectral indices. This resolution corresponds to a median resolving power of  $\lambda/\Delta\lambda = 2000$ .

As Figure 2.8 shows, this approximately matches the resolving power of modern spectrographs like those used by MUSE and SDSS. To correctly derive stellar kinematics, the MUSE spectrum would ideally be degraded to match exactly the spectral resolution as the templates. However, in order to preserve their ability to reproduce observed spectral indices, this step was not taken.

Templates within the 3200Å to 9500Å range are based on the real spectra of stars within the Milky Way taken from the STELIB spectroscopic stellar library (Le Borgne et al., 2003). STELIB is an library of around 200 empirical stellar spectra with a spectral resolution of  $\lesssim 3$ Å at a sampling of 1Å covering a relatively wide range of metallicities. While STELIB contains complete spectra for most spectral types and luminosity classes, gaps in some spectra are filled using spectra of stars with a similar spectral type.

GALEXEV uses the isochrone synthesis technique (Bruzual and Charlot, 2003b) which takes advantage of the fact that star stellar populations with some given star formation history can be expanded out into a series of starbursts. Assuming each starburst is instantaneous, it may be represented by a sum of simple stellar populations created over a period of time. The SED of a stellar population at an age,  $t$ , will be dependent on the star-formation rate density,  $\psi(t)$ , which gives the mass of stars that are formed per unit time and a metal-enrichment law,  $Z_*(t)$ . It is given by

$$F_\lambda(t) = \int_0^t \psi(t-\tau) S_\lambda(\tau, Z_*(t-\tau)) d\tau \quad (2.12)$$

where  $S_\lambda(t, Z)$  is defined in Eqn. 1.1 and  $\tau$  is the age of the SSP. In order to calculate  $S_\lambda(t, Z)$ , the Bruzual and Charlot (2003b) model interpolates an isochrone for age

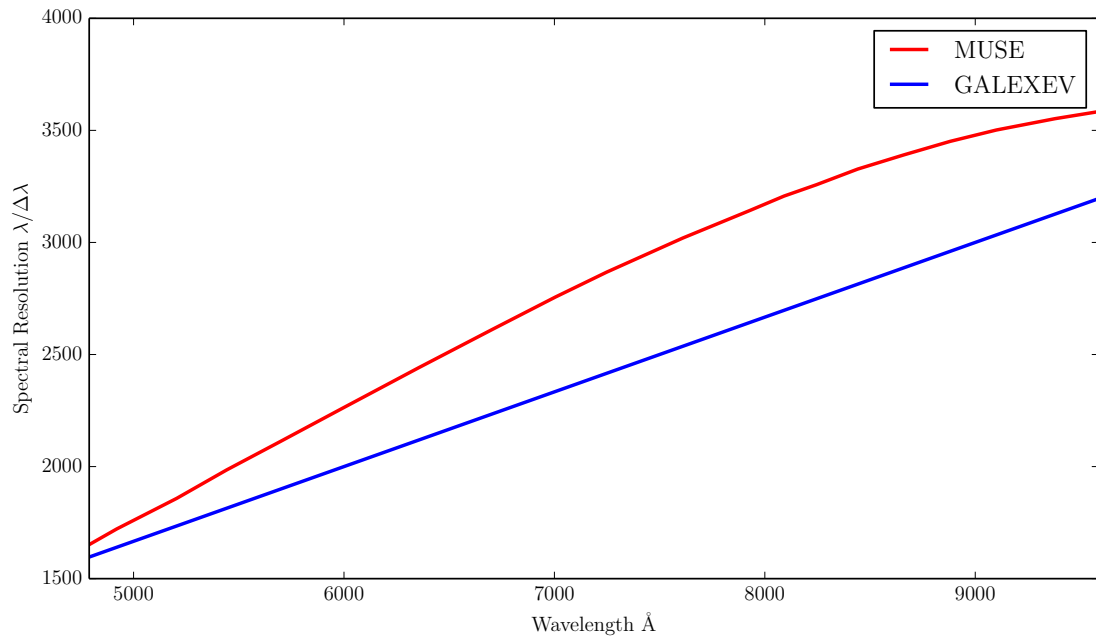


Figure 2.8: The resolving power for the MUSE spectrographs and the GALEXEV templates. The MUSE spectral resolution curve is measured using calibration arc lamps (HgCd, Xe, Ne). The data for MUSE is taken from the MUSE user manual (Richard and Bacon, 2015).

$\tau$  using stellar isochrone tracks along the Hertzsprung-Russell diagram. Bruzual and Charlot (2003b) populate each evolutionary step along the stellar isochrone with stars from the STELIB empirical spectral library for the 3200Å to 9500Å range. For the entire range from 91Å and  $1.6 \times 10^6$ Å, lower spectral resolution theoretical and observational stellar libraries are used.

Finally, the SED for each SSP is mass normalised so that at an age of  $\tau = 0$  each SSP represents a total stellar mass of  $1M_{\odot}$ .

## 3 Simple approach

As a point of comparison, we first perform SED fitting for NGC 7742 using the spectroscopic data points from MUSE only and the photometric data points from GALEX and SDSS only. The fits were performed using a modified version of the GANDALF (Sarzi et al., 2006) SED fitting code. NCG 7742 was split into apertures for the bulge, ring and disk and then fit using the two different methods.

### 3.1 GANDALF

GANDALF (Gas AND Absorption Line Fitting) (Sarzi et al., 2006) is an SED fitting code which is able to separate the stellar continuum from emission nebula due to ionised gas using the spectra of nearby galaxies and also measure gas emission and line kinematics.

Typically, the fit takes place in two stages. Initially, stellar kinematics need to be derived using a library of stellar templates which are interpolated to the same logarithmic wavelength steps as the spectrum of the object (while conserving the flux). Regions of the spectrum potentially affected by gas emission or sky line emission are masked and the stellar templates are fit with the observed spectrum. Stellar kinematics are determined by convolving the templates with the line of sight velocity distribution modeled as a Gauss-Hermite series. Least squares fitting minimisation is used to calculate the best fit parameters for the template weights and for the stellar kinematics: the mean velocity of the Gaussian,  $v_{fit}$ , its dispersion,  $\sigma$ , plus the Hermite coefficients,  $h_3$  to  $h_M$  as discussed in §1.4.3.

In order for the dispersions that are derived to be meaningful, the spectra should be convolved to the spectral resolution of the templates. As explained in §2.5, this would mean that spectral indices can not be properly fit. As a result, this step is skipped, as recovering stellar kinematics is not central to our study. It is more important that the spectral indices for the template and the spectrum can be made to fit.

A second fit is then performed. First the input LOSVD, calculated in the first step, is used to convolve the input templates with the derived stellar kinematics. These convolved SSP models are fit along with Gaussian emission line templates for the ionised gas emission. Both the SSP templates and the emission line templates are reddened according to the Calzetti attenuation law (Calzetti et al., 2000). This law adopts a foreground screen dust model. GANDALF searches simultaneously for the optimal combination of stellar templates, velocities and dispersions of each of the Gaussian templates as well as separate reddening parameters for the line emission and stellar templates. The model, incorporating the reddened stellar and gas emission templates is evaluated and compared to the observed galactic spectrum. Its parameters are minimised using least squares fitting.

After it has completed the fit, GANDALF outputs an array containing the best fitting velocity, dispersion, flux and amplitude for each emission line template, the values for each template weight and an array containing the best fit model spectrum to the observed spectrum.

Alterations to the GANDALF code are described later in this section.

## 3.2 Apertures

In order to explore star formation history spatially, NGC 7742 was split into a number of apertures. These apertures include annuli for the bulge, the nuclear ring and the disk of NGC 7742. These radii of these apertures were decided upon visually by examining images extracted from the MUSE datacube. Images of NGC 7742 for example at the wavelength of the [OIII] line can be used to get a better idea of the boundaries of the starburst ring. Since the [OIII] transition requires stars with  $T_{\text{eff}} > 36000\text{K}$ , we know that regions which are bright in [OIII] have ongoing star formation. Figure 3.1 shows the apertures chosen for the bulge, ring and disk.

In order to find the flux within each aperture, the total number of counts within that aperture are summed. We also need to know the scale of the image in terms of arcseconds per pixel in order that the aperture can be made to enclose the correct area of the image. To find the total flux in the aperture, first the centre of the galaxy has to be located on the image. This is done visually. The  $x$  and  $y$  co-ordinates of the image are then defined such that the centre of the galaxy lies at  $(0, 0)$ . It is then simple to define the apertures using  $r = \sqrt{x^2 + y^2}$ , the pixels which are contained in each aperture are those that lie at a radius between  $r_i$  and  $r_j$ . The sum of the pixels within these apertures gives the total number of counts within the aperture and these counts can then be converted to flux densities as detailed in §2.

For the MUSE spectra, a similar approach was taken, however the pixels in each

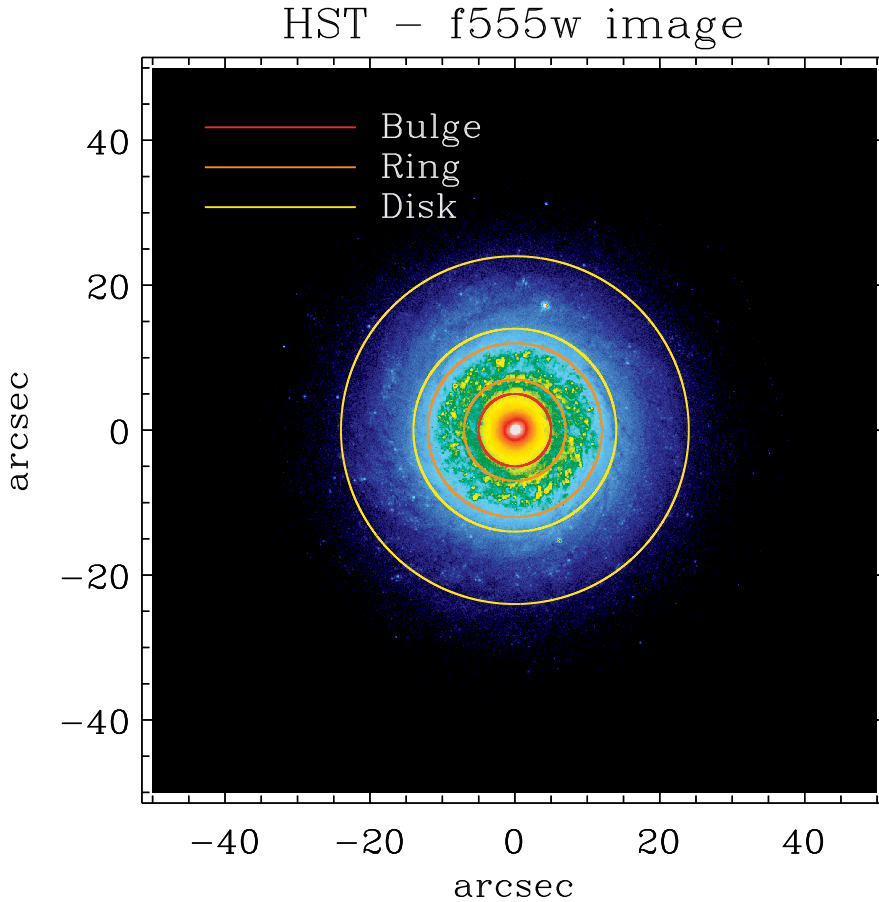


Figure 3.1: HST image of NGC7742 with apertures for the bulge, ring and disk plotted.

aperture were summed over the wavelength axis of the datacube so that a spectrum with the same number of elements as the wavelength axis is produced.

The tables below (Table 3.1 to Table 3.3) give the minimum radius,  $r_i$  and the maximum radius,  $r_j$ , for each aperture used in terms of arcseconds and in terms of pixels for GALEX, SDSS and MUSE.

GALEX (1.5“/pixel)	$r_i$ [arcsec]	$r_j$ [arcsec]	$r_i$ [pixels]	$r_j$ [pixels]
Bulge	0	5	0	3.33
Ring	7	12	4.67	8.00
Disk	14	24	9.33	16.00

Table 3.1: Minimum and maximum radius of the annuli in arcseconds and pixels for GALEX.

SDSS (0.396“/pixel)	$r_i$ [arcsec]	$r_j$ [arcsec]	$r_i$ [pixels]	$r_j$ [pixels]
Bulge	0	5	0	12.63
Ring	7	12	17.68	30.30
Disk	14	24	35.35	60.61

Table 3.2: Minimum and maximum radius of the annuli in arcseconds and pixels for SDSS.

MUSE (0.2“/pixel)	$r_i$ [arcsec]	$r_j$ [arcsec]	$r_i$ [pixels]	$r_j$ [pixels]
Bulge	0	5	0	12.63
Ring	7	12	17.68	30.30
Disk	14	24	35.35	60.61

Table 3.3: Minimum and maximum radius of the annuli in arcseconds and pixels for MUSE

### 3.3 Flux Densities

The following tables give the counts and their corresponding errors for GALEX and SDSS.

	GALEX	FUV	NUV
Bulge	$0.88350 \pm 0.0243$	$5.9072 \pm 0.0630$	
Ring	$11.673 \pm 0.0883$	$47.4493 \pm 0.1781$	
Disk	$5.3496 \pm 0.0608$	$25.4452 \pm 0.1320$	

Table 3.4: Counts for each aperture in terms of photons per second and their error for GALEX in FUV and NUV detectors.

	GALEX	FUV	NUV
Bulge	$1.2415 \times 10^{-15} \pm 5.5350 \times 10^{-18}$	$1.1631 \times 10^{-15} \pm 2.8794 \times 10^{-18}$	
Ring	$1.6403 \times 10^{-14} \pm 1.1574 \times 10^{-16}$	$9.3242 \times 10^{-15} \pm 3.5073 \times 10^{-17}$	
Disk	$7.6716 \times 10^{-15} \pm 8.5376 \times 10^{-17}$	$5.0100 \times 10^{-15} \pm 2.5950 \times 10^{-17}$	

Table 3.5: Flux densities and their error calculated from the counts in Table 3.4.

	SDSS	u	g	r	i	z
Bulge	535.799	2634.79	5396.09	7659.57	9988.45	
Ring	1348.52	3478.28	5862.25	7369.57	9192.60	
Disk	920.642	3134.36	5796.47	8146.19	10044.2	

Table 3.6: Counts for each aperture in nanomaggies for each SDSS filter.

	SDSS	u	g	r
Bulge	$4.1969 \times 10^{-15} \pm 1.3799 \times 10^{-16}$	$1.2880 \times 10^{-14} \pm 1.2520 \times 10^{-16}$	$1.5351 \times 10^{-14} \pm 9.4610 \times 10^{-17}$	
Ring	$9.7799 \times 10^{-15} \pm 2.1858 \times 10^{-16}$	$1.7004 \times 10^{-14} \pm 1.4432 \times 10^{-16}$	$1.6677 \times 10^{-14} \pm 9.8870 \times 10^{-17}$	
Disk	$8.5917 \times 10^{-15} \pm 2.6522 \times 10^{-16}$	$1.5323 \times 10^{-14} \pm 1.3943 \times 10^{-16}$	$1.6490 \times 10^{-14} \pm 9.9416 \times 10^{-17}$	
SDSS	i		z	
Bulge	$1.4825 \times 10^{-14} \pm 7.8157 \times 10^{-17}$	$1.3540 \times 10^{-14} \pm 6.2921 \times 10^{-17}$		
Ring	$1.4263 \times 10^{-14} \pm 7.7993 \times 10^{-17}$	$1.2461 \times 10^{-14} \pm 6.1147 \times 10^{-17}$		
Disk	$1.5766 \times 10^{-14} \pm 8.6700 \times 10^{-17}$	$1.3615 \times 10^{-14} \pm 6.6692 \times 10^{-17}$		

Table 3.7: Flux densities and their error calculated from the counts in Table 3.6.

## 3.4 Method

In order to make the data consistent with each other, the point spread function of each image had to be found by fitting a Gaussian to a point source in the image. The images were then convolved to the same angular resolution. In the case of photometric data, the GANDALF code was modified to perform bandpasses of the SSP templates, so that photometric fluxes could be modeled. Finally the code was altered so that additional reddening was applied to young SSP templates in order to account for birth cloud attenuation.

### 3.4.1 Convolution of data

In order that they can be correctly compared, the SDSS, GALEX and MUSE data must all be convolved to the same angular resolution. To do this we first need to know the angular resolution for each image. Each image will need to be convolved with a Gaussian PSF that is the quadratic difference between its own angular resolution and the angular resolution of the worst image.

The intrinsic spatial distribution of the photon counts for an object are changed by the point spread function (PSF) of the imaging system. The resulting image is blurred by the PSF so that the counts are spread out, this means that brighter areas of the object appear less bright as counts are spread out into dimmer areas, which become less dim. Mathematically speaking, the image,  $I'$ , seen by the imaging system is the intrinsic image,  $I$ , convolved with a PSF which is can usually be approximated by a Gaussian kernel so that

$$I'(x) = I(x) \star \text{PSF}(x) \quad (3.1)$$

The point spread function of an instrument is a measure its resolving power. The full-width-half-maximum of the PSF gives the minimum angular separation at which it is still possible to resolve two point sources.

The PSF of ground based telescopes like the VLT and SDSS are dominated by the turbulence of the atmosphere and are called 'seeing limited' systems. Compared with the PSF due to seeing, which is around  $0.5''$  FWHM in ideal conditions and at high altitude, the PSF of the telescopes optics, which has a median value of only  $\sim 0.05''$  FWHM for SDSS, will be negligible to first order.

Because there is no atmosphere obstructing the line of sight, space based telescopes like GALEX are theoretically limited by the properties of the imaging system itself. Optical systems like this are called diffraction limited systems because their angular resolution depends to a significant degree only on the size of the aperture and the

wavelength of light. GALEX is not, in fact diffraction limited and its angular resolution is significantly larger than the theoretical diffraction limited resolution (Morrissey et al., 2007). This is largely due to the detectors and to a lesser extent, imprecisions in calibration of the aspect correction (Morrissey et al., 2005).

The PSF of the imaging system is defined by the normalised response of the system to a point source,  $\delta$ , so the image of a point source yields the PSF of the imaging system recording the image.

$$\delta(x) \rightarrow \text{PSF}(x) \cdot \int \text{PSF}(x) dx \quad (3.2)$$

This means that the PSF of each instrument can be found by from an unresolved, point source in the image, which will be spread out by the PSF.

For the ground based telescopes, SDSS and VLT/MUSE, we need to consider the seeing in addition to the point spread function due to the properties of the instrument itself. MUSE takes spectra in each wavelength bin simultaneously and, as Figure 2.4 shows, SDSS records a different strip of the sky in each filter simultaneously. We assume that seeing for SDSS does not change dramatically during the 60 seconds separating the point at which the following filter begins its exposure of the part of sky that the previous filter just completed. If this is the case, the PSF of a foreground star in SDSS is approximately constant across all bands since the difference between filters due to diffraction is not significant compared with an ideal seeing of 0.5" FWHM. It is correct, then, to use an average value of the FWHM of the PSF for both SDSS and MUSE.

To find the PSF for both the MUSE and SDSS data we approximate the PSF as a Gaussian. By selecting an unresolved foreground star and setting the centre of the star to  $r = 0$  in the image, we can plot the intensity of about the centre point as a function of radius out to a certain radius. This is done for each band in SDSS and for each wavelength bin in MUSE.

We can then fit a Gaussian plus a background level to these points so that we can recover the dispersion of the PSF. The function that is fitted has the form

$$g(r) = A_0 e^{-\frac{1}{2} \left( \frac{r-A_1}{A_2} \right)^2} + A_3 \quad (3.3)$$

where we are interested in the parameter  $A_2$  which is the standard deviation of the Gaussian  $\sigma$ , a measure of its dispersion. Figure 3.2 shows the fits for four of the SDSS bands.

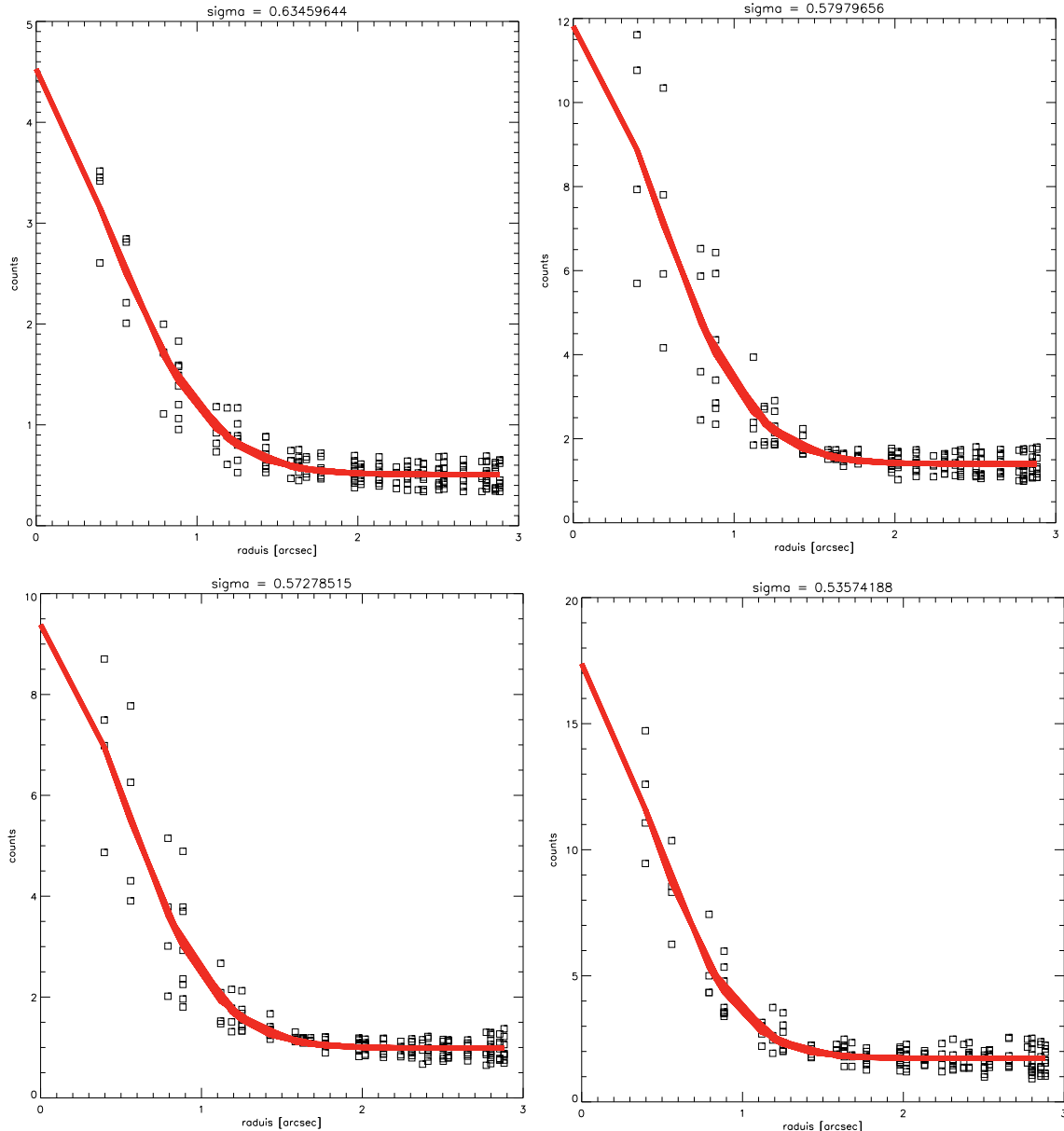


Figure 3.2: Gaussian fits to a foreground star in g, i, r and z bands of the SDSS images for NGC 7742.

The dispersion,  $\sigma$ , was calculated for each wavelength bin in the MUSE data giving

a value of  $0.2895'' \pm 0.017''$ . In terms of its FWHM<sup>1</sup> this is  $0.6817''$ . Likewise,  $\sigma$  was calculated for each SDSS band. The mean value of  $\sigma$  for SDSS is  $0.5978''$ , and the standard error on the mean is  $0.0233''$ . This corresponds to a FWHM of  $1.4''$ .

In order to degrade each image, they are each convolved with a normalised Gaussian kernel. This Gaussian has a dispersion of  $\sigma = \sqrt{\sigma_{\text{NUV}}^2 - \sigma_{\text{Image}}^2}$ , the quadratic difference between the GALEX NUV angular resolution and the image's angular resolution in terms of standard deviation of the PSF. The Gaussian kernel has the same pixel dimensions as the image and has the form

$$g(x, y) = \frac{1}{2\pi\sigma^2} e^{-\frac{(x-x_0)^2+(y-y_0)^2}{2\sigma^2}} \quad (3.4)$$

where  $x_0$  and  $y_0$  are the central  $x$  and  $y$  co-ordinates of the image. The Gaussian is normalised by the constant,  $1/2\pi\sigma^2$ , resulting in a total area of 1. The new, degraded image is given by the convolution of the image with the kernel

$$I'(x, y) = I(x, y) \star g(x, y) \quad (3.5)$$

Since the area under the Gaussian is normalised to 1, the total flux within the image is conserved. However, flux may be smeared outside of the apertures, reducing the total flux in the convolved versus the unconvolved apertures.

Figure 3.3 shows an image of NGC 7742 in FUV unconvolved and convolved to the angular resolution of the GALEX NUV image. Both images use the same colour scale, so we can see that the flux in the bulge has been spread out into other regions since its colour has become cooler.

---

<sup>1</sup>The full-width-half-maximum dispersion of a Gaussian is  $2\sqrt{2 \ln 2}\sigma$ .

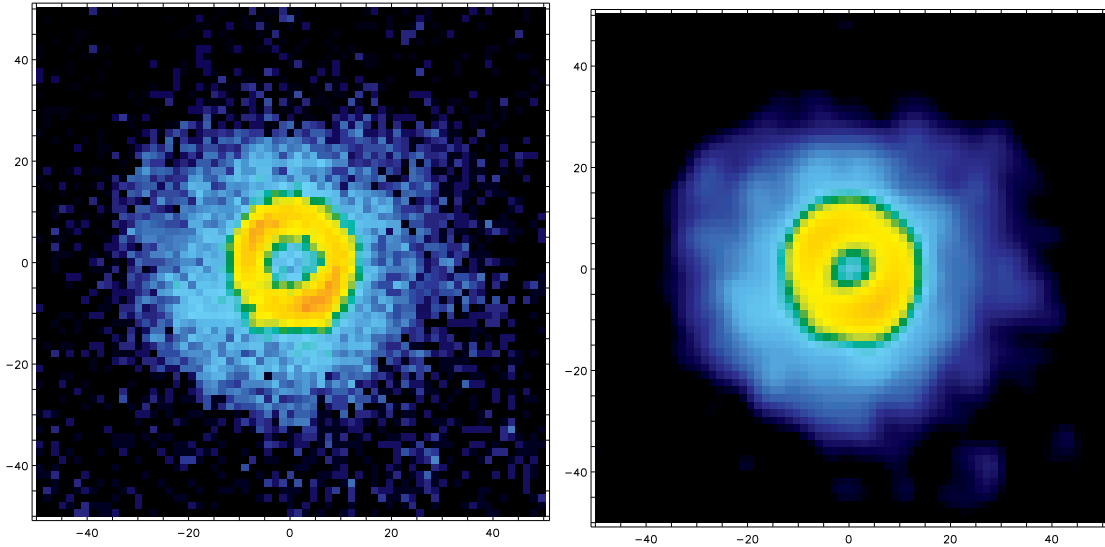


Figure 3.3: Image of NGC 7742 in FUV GALEX band unconvolved and convolved. The second image shows the first image convolved by a Gaussian with a FWHM of  $\sqrt{5.3^2 - 4.2^2}$ .

### 3.4.2 Corrected Flux Densities

The following tables give the corrected counts and their corresponding errors for GALEX and SDSS images convolved to the GALEX NUV angular resolution. We can see that, compared with the unconvolved fluxes previously, the convolution results in brighter regions of the galaxy losing flux and the flux of dimmer regions increasing. This is because the amount of flux that is spread out of a brighter region will be greater than the amount spread into that region by a neighboring, dimmer region.

	GALEX	FUV	NUV
Bulge	$1.0965 \pm 0.0270$	$5.9072 \pm 0.0630$	
Ring	$10.7426 \pm 0.0847$	$47.4493 \pm 0.1781$	
Disk	$5.7617 \pm 0.6240$	$25.4452 \pm 0.1320$	

Table 3.8: Counts from the convolved images for each aperture in terms of photons per second and their error for GALEX in FUV and NUV detectors.

	GALEX	FUV	NUV
Bulge	$1.5410 \times 10^{-15} \pm 7.2469 \times 10^{-18}$	$1.1631 \times 10^{-15} \pm 2.8794 \times 10^{-18}$	
Ring	$1.6095 \times 10^{-14} \pm 1.1900 \times 10^{-16}$	$9.3242 \times 10^{-15} \pm 3.5073 \times 10^{-17}$	
Disk	$8.0961 \times 10^{-15} \pm 8.7675 \times 10^{-17}$	$5.0100 \times 10^{-15} \pm 2.5950 \times 10^{-17}$	

Table 3.9: Flux densities and their error calculated from the counts in Table 3.8.

	SDSS	u	g	r	i	z
Bulge	500.259	2344.99	4763.01	6727.51	8731.58	
Ring	1159.45	3237.40	5631.36	7287.25	9187.75	
Disk	985.111	4275.82	6008.63	8390.02	10349.8	

Table 3.10: Counts from the convolved images for each aperture in nanomaggies for each SDSS filter.

SDSS	u	g	r
Bulge	$4.1969 \times 10^{-15} \pm 1.3799 \times 10^{-16}$	$1.1120 \times 10^{-14} \pm 1.1636 \times 10^{-16}$	$1.3618 \times 10^{-14} \pm 8.9132 \times 10^{-17}$
Ring	$9.7799 \times 10^{-15} \pm 2.1858 \times 10^{-16}$	$1.5705 \times 10^{-14} \pm 1.3876 \times 10^{-16}$	$1.5989 \times 10^{-14} \pm 9.6826 \times 10^{-17}$
Disk	$8.5917 \times 10^{-15} \pm 2.6522 \times 10^{-16}$	$1.6191 \times 10^{-14} \pm 1.3876 \times 10^{-16}$	$1.7100 \times 10^{-14} \pm 1.0118 \times 10^{-17}$
SDSS	i		z
Bulge	$1.3000 \times 10^{-14} \pm 7.3263 \times 10^{-17}$	$1.1845 \times 10^{-14} \pm 5.8902 \times 10^{-17}$	
Ring	$1.4128 \times 10^{-14} \pm 7.7642 \times 10^{-17}$	$1.2466 \times 10^{-14} \pm 6.1161 \times 10^{-17}$	
Disk	$1.6273 \times 10^{-14} \pm 8.7886 \times 10^{-17}$	$1.4032 \times 10^{-14} \pm 6.7590 \times 10^{-17}$	

Table 3.11: Flux densities and their error calculated from the counts in Table 3.10.

### 3.4.3 Photometric fluxes

In order to fit the observed flux we need to be able to calculate the flux of each template in some given passband. In order to do this, we first need to ensure that the wavelength range of the templates is adequate to cover the wavelength range of the passbands used. In the case of the GALEX and SDSS passbands, the templates must cover 1340 Å (minimum of the GALEX FUV band) to 10833Å (maximum of the SDSS z band). Some filters used cover wavelengths lying outside of the 3200Å to 9500Å of the high resolution GALEXEV templates. However, all of the filters are covered by the lower resolution 91Å to  $1.6 \times 10^6$ Å range. The coarser sampling is unlikely to introduce significant uncertainty to the fits because the passbands used are still wide compared with the spectral resolution of the templates.

By initially performing a bandpass on each template, we can find the flux density within some given passband. The associated flux densities per each bandpass and per each template can then treated in much the same way as the spectroscopic flux densities: During the fitting process, the observed average photometric flux densities are appended onto the end of the array containing the observed galactic spectrum. Likewise, the average flux density in each bandpass is calculated for each template and then appended to the array for that template.

In order to calculate the average flux density in a bandpass, response curves from the Spanish Virtual Observatory filter profile service are used. A catalogue of filter responses is provided and can be queried using a filter ID or instrument name. The response curve can be downloaded as a two column ASCII data file containing a list of wavelengths and transmissions.

The response curve of each filter is the transmission through the filter as a function of wavelength but the definition of transmission depends on the type of detector that is used by the telescope. A detector is either an 'energy counter' or a 'photon counter' and the transmission of the filter for each type of detector is given as the fraction of incident energy that the filter allows through or the fraction of incident photons respectively. SDSS and GALEX are both photon counting instruments, however, the photon counts were converted fluxes in terms of energy when calibrated, so the energy counter definition for transmission is used. The bandpass signal,  $T(\lambda) S_\lambda$ , is the signal seen by the detector after it has passed through the filter: the transmission multiplied by the spectrum of the template. The average flux density within a passband is recovered by dividing the total bandpass signal by the area under the response curve. Using the energy counter definition this is:

$$F_\lambda = \frac{\int_{\lambda_{\min}}^{\lambda_{\max}} T(\lambda) S_\lambda d\lambda}{\int_{\lambda_{\min}}^{\lambda_{\max}} T(\lambda) d\lambda} \quad (3.6)$$

where  $T(\lambda)$  is the transmission of light through the filter as a function of wavelength,  $S_\lambda$  is the spectrum of the template in terms of its flux density.

Because the light from the galaxy will be Doppler shifted, it is necessary to be aware that the wavelengths corresponding to each of the flux density bins of the raw stellar templates are correct in the case of the rest-frame of the galaxy only. The wavelength array for either the filter response curve or for each template needs to be shifted according to the mean velocity of the galaxy so that the same part of the spectrum is integrated over for the observed object in each filter.

Programmatically, the average flux density is calculated by multiplying a filter response array with a template spectrum array. To do this, the wavelength array for the response curve is shifted according to the central velocity calculated by the initial fit. The Doppler redshift,  $Z$ , is approximately  $v/c$  as long as  $\gamma \approx 1$ , which will be the case for all nearby galaxies. The simplest way to do this is to shift the array containing the wavelengths for the filter response by multiplying it by  $1 - Z$ :  $\lambda' = \lambda(1 - Z)$ . It is not necessary to convolve the templates at this point as broadening of the spectrum will make only a negligible change to the flux contained within the bandpass.

The filter's response curve is then interpolated so that it has the same steps and number of elements as the template spectrum. It is also necessary to ensure that any elements of the interpolated response curve outside of the range of the original response curve are equal to 0. If the template spectrum and interpolated response curve are then multiplied elementwise, we obtain the flux density allowed to pass through the filter for each wavelength bin of the spectrum. The total flux flux density within the passband (i.e. the total that is allowed to pass through the filter) is just the total of this array. By then dividing by the total of the interpolated response curve, we obtain the average flux density of the template in a given bandpass. The photometric fluxes are appended onto the template array so they match the array containing the observed data for the galaxy.

These photometric fluxes are ignored during the initial fit to determine stellar kinematics and then included in the final GANDALF fit. Currently, the Gaussian emission line templates are ignored when fitting the photometry because the template fluxes are calculated before the final fit, which does include gas emission.

### 3.4.4 Additional Reddening

As mentioned in 1.4.2, young stellar populations are subject to 'birth cloud' attenuation or 'internal reddening' at ages of  $t \lesssim 10$  Myrs, after which they will have left the birth cloud (Walcher et al., 2010). Young stars, which remain embedded in their birth material are attenuated both by the diffuse gas of the ISM and the stellar birth cloud. To correctly account for this, another  $E(B - V)$  parameter is required. This parameter is used to further redden young SSPs.

Each time the galactic SED model is evaluated during the final fit, all SSP templates and Gaussian emission templates are attenuated according to the current value of the  $E(B - V)$  parameter and the  $E(B - V)_{\text{internal}}$  parameter respectively. For both templates, the Calzetti attenuation law is used and the templates are divided by an array matching the wavelength range of the templates. This is calculated using  $10^{-0.4(E(B-V)_*k(\lambda))}$  where  $k(\lambda)$  is the reddening curve calculated from the Calzetti law as a function of wavelength.

To introduce additional attenuation for young SSP templates, the code was altered so that templates with ages under 10 Myrs are also attenuated a second time, this time according to the  $E(B - V)_{\text{internal}}$  parameter which is also tied to the Balmer decrement.

If this was not the case, the fit would yield drastically fewer young stars, as a smaller weight would need to be applied to a young template to give the same flux as the same template that has received additional internal reddening.

## 3.5 MUSE spectrum only

Fits were performed for the spectra of the bulge, ring and disk of NGC 7742 which were extracted from the MUSE datacube. Below we present the results of the GANDALF fits using the MUSE spectrum only. Figure 3.4 shows the fits in pixel space for the bulge, ring and disk of NGC 7742. The residuals, in blue, give the difference between the observed spectrum and the best fit spectrum for the unmasked parts of the spectrum. Where the residuals are not plotted, the spectrum has been masked.

For all of the fits, at no point do the residuals jump significantly above their average level, indicating that there is no difficulty fitting to any particular unmasked part of the spectrum.

Figure 3.5 shows the fits for the bulge, ring and disk extrapolated out to the UV. The full length GALEXEV templates were multiplied by their best fit weights and then reddening was applied. Gaussian emission line templates are not included, so this figure indicates only the contribution by stars to the integrated light from the galaxy.

We see that, in the UV, the predicted observed flux density for the bulge drops dramatically. The flux density for the ring increases steadily up to the Lyman limit at

912Å. Correspondingly, there is an increase for the disk as well, however its gradient is more shallow.

Table 3.13 shows the best fit parameters for the GANDALF fit. The templates given a non-zero weight are shown with their age, metallicity and their value as a fraction of the total of the parameter values. Because each template corresponds to an initial mass of  $1M_{\odot}$  in stars, the fractions indicate the relative mass of stars contributed by each template. Table 3.12 shows  $\chi^2$  value for the fit and the values for the two E(B – V) values.

Region	$\chi^2$	E (B – V)	E (B – V) <sub>internal</sub>
Bulge	603076	0.157	0.129
Ring	1170127	0.215	0.142
Disk	3372265	0.257	0.263

Table 3.12:  $\chi^2$  value of the best fit and attenuation parameters for each region of NGC 7742 for spectrum-only fit.

Region	Age (Gyrs)	Metallicity (Z)	Fraction
Bulge	1.0	0.05	0.0841
	1.12	0.05	0.851
	3.16	0.0004	0.0647
Ring	0.003	0.004	0.0104
	0.79	0.008	0.0744
	1.0	0.05	0.812
	2.51	0.0004	0.103
Disk	0.003	0.004	0.0240
	0.89	0.05	0.857
	1.0	0.05	0.119

Table 3.13: SSP template weights of non-zero values for spectrum-only fit.

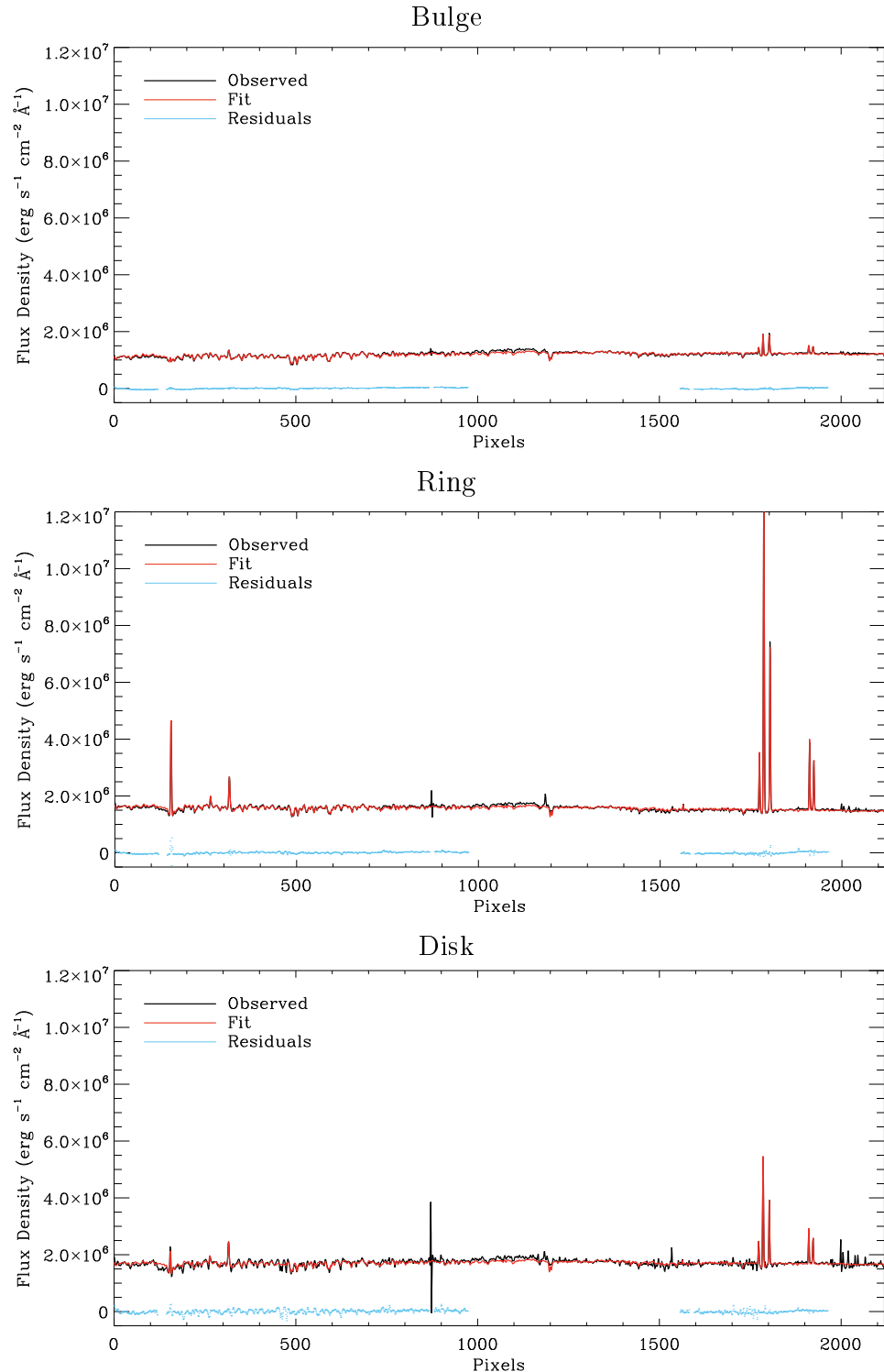


Figure 3.4: Comparison in pixel space between the observed and best fit spectrum, which includes the stellar templates and Gaussian emission templates. Flux density is multiplied by  $10^{20}$ .

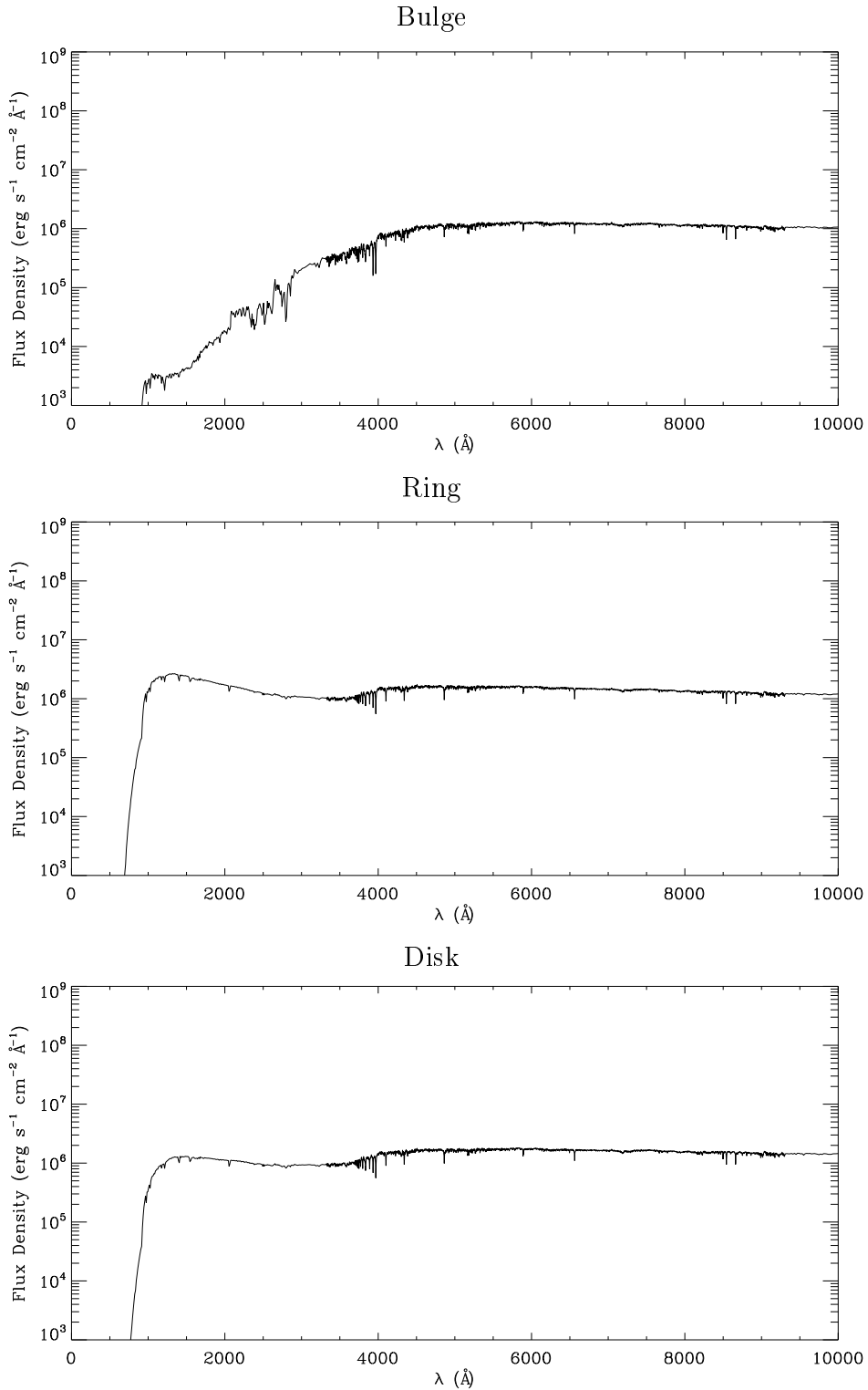


Figure 3.5: Fit extrapolated to the UV. Shows the predicted contribution to the observed galactic SED by stars only.

### 3.6 Photometry only

Fits were also performed for photometric GALEX and SDSS data for the bulge, ring and disk of NGC 7742. For the fit with photometry only, the templates were not convolved by the LOSVD, only shifted according to the redshift of the galaxy. Clearly, it is not possible to derive the LOSVD from photometry only because of the sparse sampling, but broadening the templates also would have no effect on the fit, since any broadening is insignificant compared with the width of the passband. Below we present the results of the GANDALF fits using the GALEX and SDSS photometry only. Figure 3.6 shows the fits for the bulge, ring and disk of NGC 7742 extrapolated using the best fit templates. The photometric data points are indicated by blue diamond markers.

Since we have data in the UV for the photometry, the fit in the UV should more like the true SED of NGC 7742. However, it is difficult to trust either the template weight parameters or the  $E(B - V)$  parameters. The Balmer decrement can't be used to derive  $E(B - V)$  values and there are no absorption line indices to constrain stellar metallicity. This means we have no way of breaking the metallicity-age degeneracy or the reddening-age degeneracy, so the best fit parameters will be unreliable.

Table 3.15 shows the best fit parameters for the GANDALF fit. The templates given a non-zero weight are shown with their age, metallicity and their value as a fraction of the total of the parameter values. We can see that due to the reddening-age degeneracy, GANDALF has produced some very unphysical fits. For example in the disk the fit indicates 26.6% of stars are 2.5Myrs old, it is obviously impossible that one quarter of the stellar mass in the disk was formed in the last 2.5Myrs.

Table 3.14 shows  $\chi^2$  value for the fit and the values for the two  $E(B - V)$  values. We can see that, compared with the spectroscopic fit, the  $E(B - V)$  are completely different. The  $\chi^2$  values indicate the goodness of fit between the observed spectrum and the predicted spectrum, exactly as they did in the previous spectroscopic fit. The  $\chi^2$  values are around 50 times larger than for the spectroscopic fit, indicating that the photometry only fit does not produce a good fit to the observed spectrum.

Region	$\chi^2$	$E(B - V)$	$E(B - V)_{internal}$
Bulge	24285207	0.1	0.0
Ring	65649256	0.0976	0.114
Disk	$1.13 \times 10^{33}$	0.1	2.141

Table 3.14:  $\chi^2$  value of the best fit for the predicted spectrum and observed spectrum with attenuation parameters for each region of NGC 7742 for photometry only fit.

Region	Age (Gyrs)	Metallicity (Z)	Fraction
Bulge	0.0025	0.0004	$7.46 \times 10^{-5}$
	0.63	0.05	0.0595
	1.26	0.05	0.223
	10.0	0.008	0.589
	10.0	0.05	0.128
Ring	0.0015	0.004	0.000198
	0.0035	0.05	0.000362
	0.018	0.05	0.00431
	0.89	0.05	0.0484
	1.0	0.05	0.0480
	7.98	0.0004	0.463
Disk	0.0025	0.0004	0.266
	0.011	0.0004	0.000295
	0.35	0.004	0.00904
	0.56	0.05	0.0235
	7.08	0.004	0.555
	10.0	0.0004	0.0146

Table 3.15: SSP template weights of non-zero values for photometry only fit.

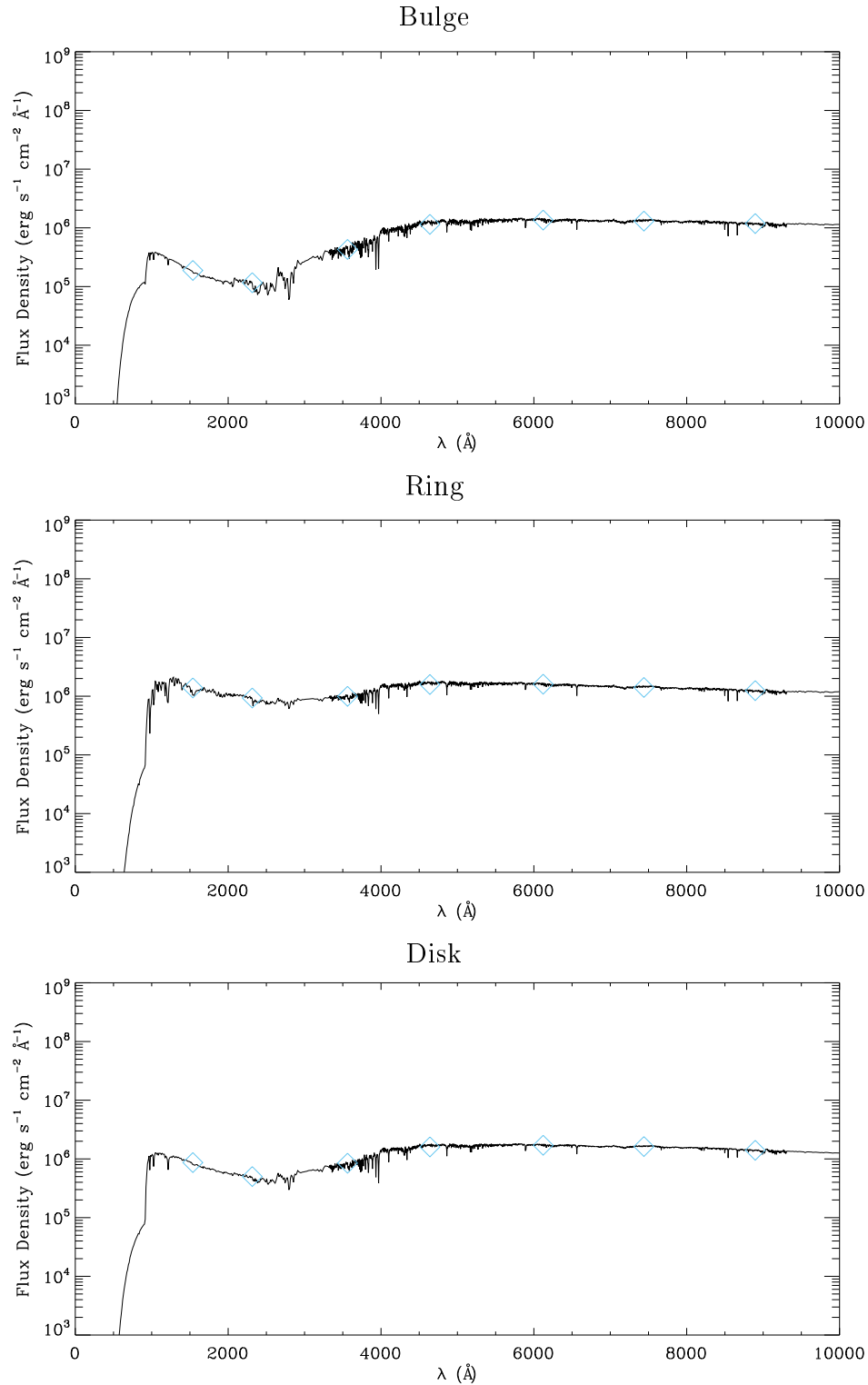


Figure 3.6: Fit extrapolated to the UV. Shows the predicted contribution to the observed galactic SED by stars only. The blue diamonds indicate the photometric data points.

## 4 Extended Approach

Following the fits using spectroscopic and photometric SEDs, fits were then performed for the bulge, ring and disk of NGC 7742 using the spectra extracted from the MUSE datacube in combination with the photometric fluxes from GALEX and SDSS images. Below we present the results of the GANDALF fits using the MUSE spectrum with GALEX and SDSS photometry. Figure 4.1 shows the fits in pixel space for the bulge, ring and disk of NGC 7742. Again, the residuals are plotted in blue and give the difference between the observed spectrum and the best fit spectrum for the unmasked parts of the spectrum.

Compared with the MUSE only fit in §3.5, the fit to the spectrum is almost identical. The  $\chi^2$  values in Table 4.1 confirm this, since the increase in the  $\chi^2$  value between the fit to the spectrum and the fit to the spectrum plus photometry is typically only 0.05%. This indicates that by fitting to the additional data points, the fit to the spectrum has not been significantly affected.

Figure 4.2 shows the template fits for the bulge, ring and disk which are created by multiplying the reddened GALEXEV templates by their assigned weight. The overall shape we see is similar to that obtained from the photometric fit. However, fine details differ between the two. For the fit to the disk, the fit prefers not to go through the NUV photometric data point, as a result there is quite a significant difference between the data point and the predicted flux density at that point. The predicted flux is around two times greater than the observed flux in NUV. It is possible that variances given by the MUSE datacube are underestimated towards the edge of the galaxy; this may mean that the errors need to be re-examined for the disk.

Table 4.2 shows the best fit parameters for the GANDALF fit. The templates given a non-zero weight are shown with their age, metallicity and their value as a fraction of the total of the parameter values. Table 3.13 shows  $\chi^2$  value for the fit between the observed spectrum and the predicted spectrum and the values for the two E(B – V) values.

The fact that the fit for the disk has not gone through the NUV data point might explain the larger weight given to young SSPs. Figure 4.2 shows that the observed NUV flux density is around 2 times smaller than the best fit predicted flux density. This may mean that the errors of the MUSE or GALEX fluxes may need to be re-examined. We see a fraction of 0.00859 for 3Myrs for the ring but the fraction is 0.0142 for the disk. We would not expect this to be the case based on, for example, the H- $\alpha$  line height, which is higher for the ring.

Region	$\chi^2$	E (B - V)	E (B - V) <sub>internal</sub>
Bulge	607105	0.161	0.142
Ring	1169377	0.190	0.172
Disk	3384121	0.221	0.274

Table 4.1:  $\chi^2$  value of the best fit for the predicted spectrum and observed spectrum with attenuation parameters for each region of NGC 7742 for spectro-photometric fit.

Region	Age (Gyrs)	Metallicity (Z)	Fraction
Bulge	0.004	0.0004	0.000485
	1.0	0.05	0.0342
	1.12	0.05	0.932
	3.16	0.0004	0.0329
Ring	0.003	0.004	0.00859
	0.79	0.008	0.0936
	1.0	0.05	0.725
	2.51	0.0004	0.173
Disk	0.003	0.004	0.0142
	0.89	0.008	0.0353
	0.89	0.05	0.836
	3.16	0.0004	0.115

Table 4.2: SSP template weights of non-zero values for the spectro-photometric fit.

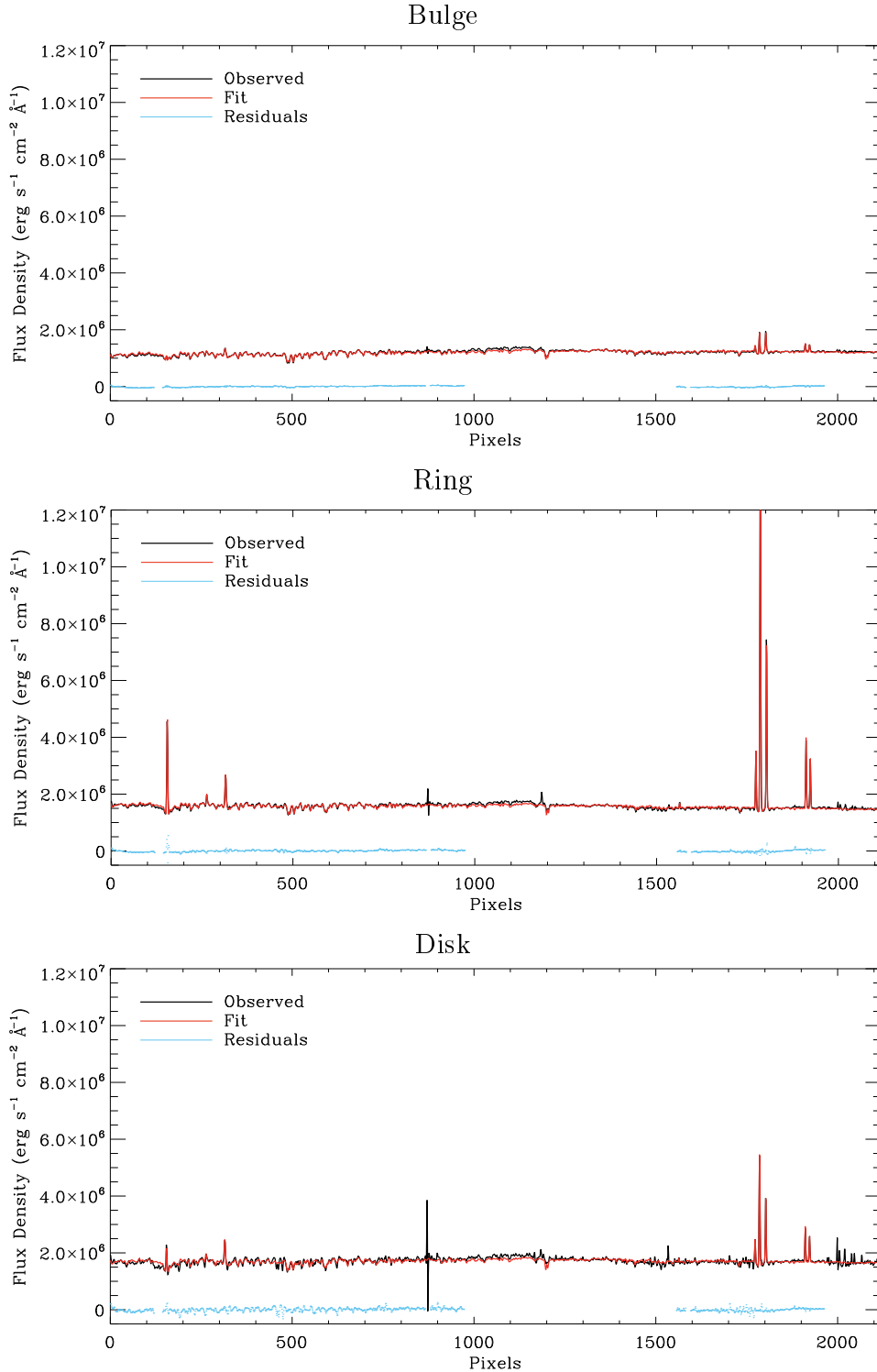


Figure 4.1: Comparison in pixel space between the observed and best fit spectrum for the spectro-photometric approach. This includes the stellar templates and Gaussian emission templates.

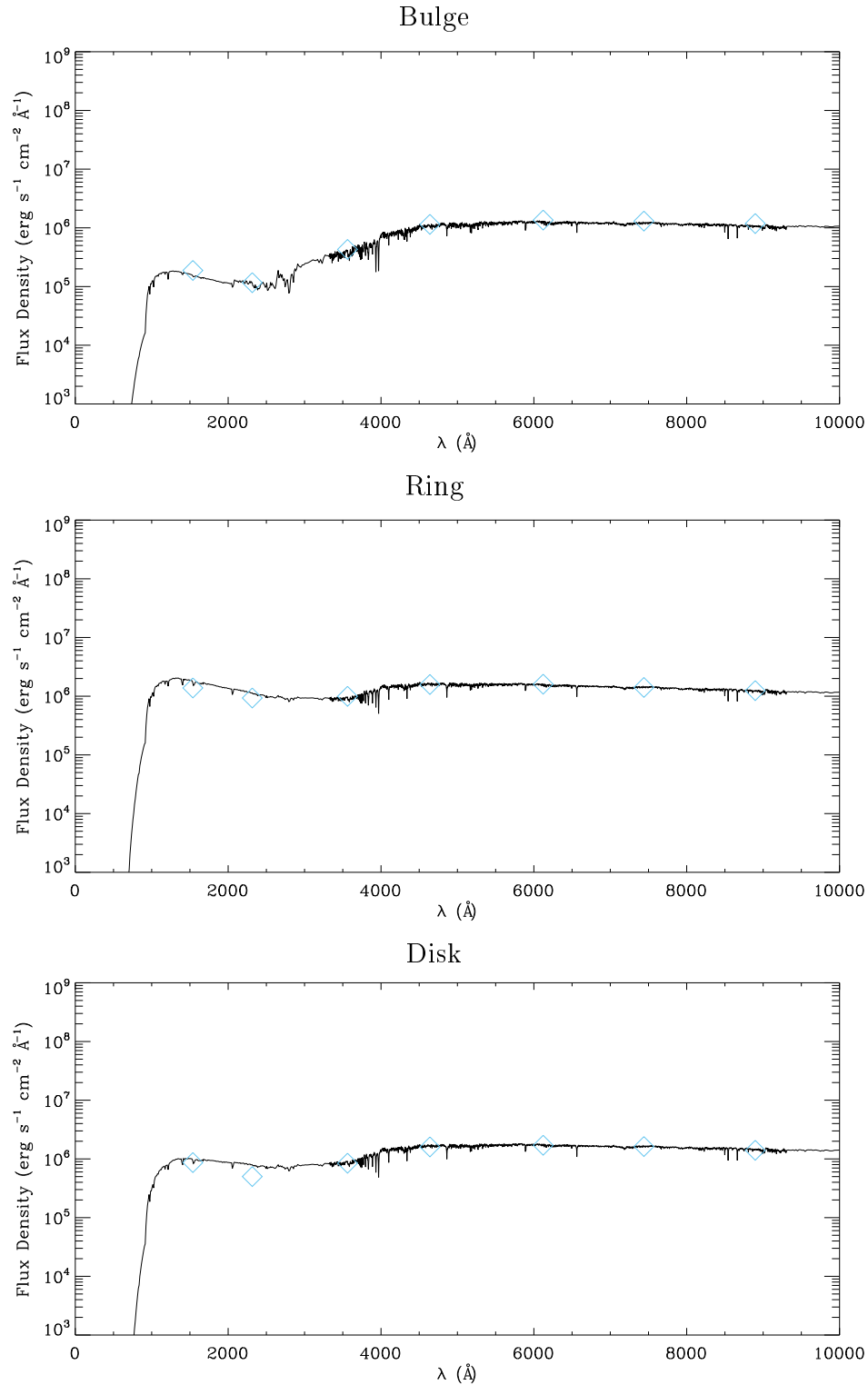


Figure 4.2: Fit extrapolated using the best fit templates. Shows the predicted contribution to the observed galactic SED by stars only. The blue diamonds indicate the photometric data points used.

## 4.1 Results

Figure 4.3 shows the spectra predicted for the spectro-photometric approach and for the spectrum only fit. We see that there are quite significant differences between both fits for all regions of NGC 7742. The bulge presents the most drastic departure of the spectro-photometric fit from the spectrum only fit. The spectrum only fit strongly under predicts the UV flux. The spectro-photometric fit in the ring differs from the fit to the spectrum by 50% to 100% in the UV region, meaning the spectroscopic fit is overestimating the UV flux. For the disk, the difference is higher, but again, the fit to the photometric data points is poor.

The discrepancy between the spectro-photometric and spectroscopic fit indicates that optical-only spectrum does not contain the information needed to constrain the UV bright population. UV data is needed to correctly predict the young population. In the case on NGC 7742, the combination of photometry and integral field spectroscopy has allowed us to better reconstruct the star formation history

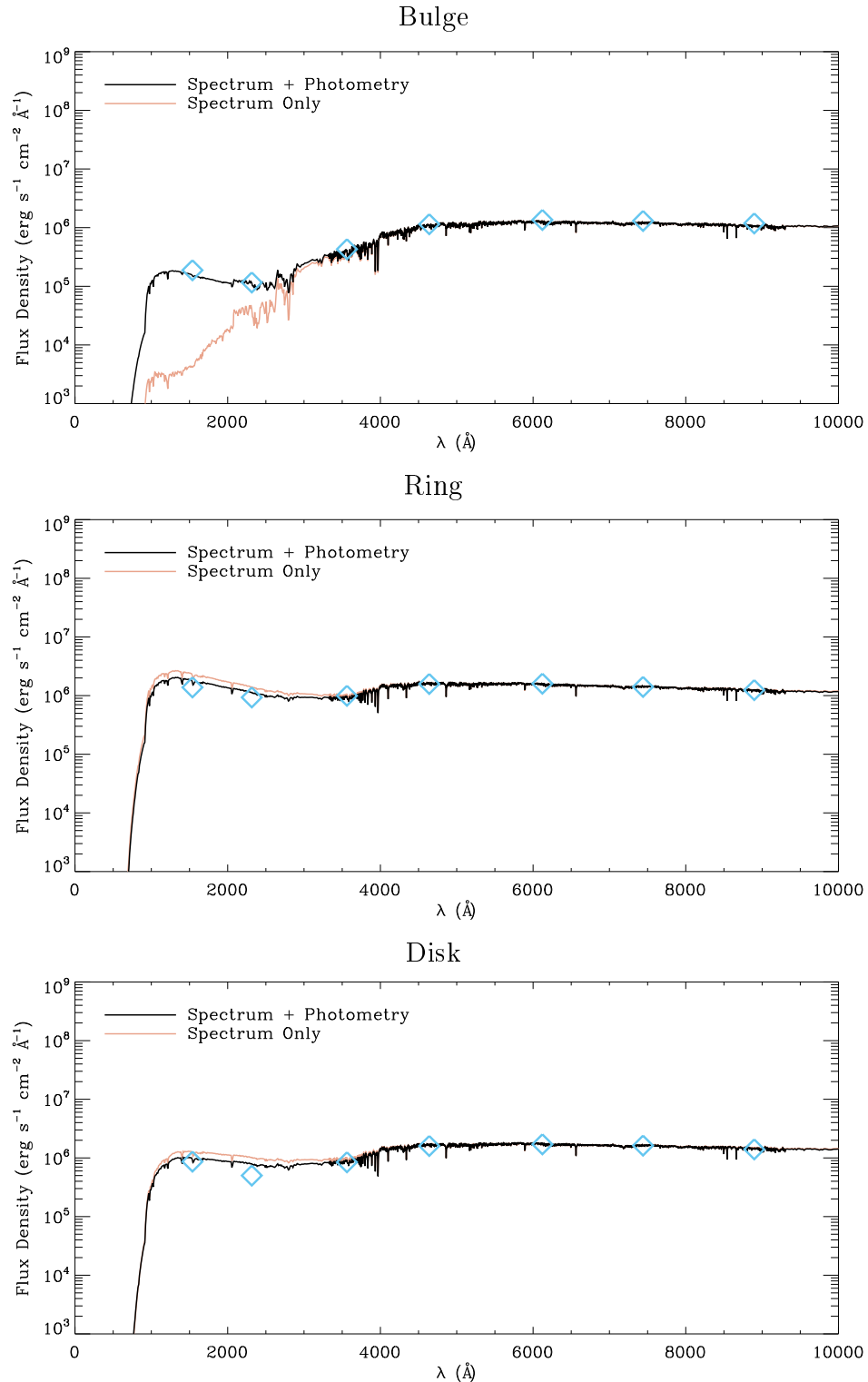


Figure 4.3: Comparison of the spectrum fits extrapolated into the UV and fits using the spectrum plus SDSS and GALEX photometry.

## 5 Errors

Once the best fit combination of parameters has been found, the solution can be perturbed in order to calculate the errors on the value of these parameters. By varying the value of a parameter,  $\theta$ , about its best-fit value, holding it at some value,  $x$ , and then refitting, we get a new  $\chi^2$  value for that point. If this is repeated many times for a grid of values, the distribution of  $\chi^2$  values as a function of parameter value,  $x$ , can be used to calculate the error on the best-fit value.

First, an initial fit is made with no conditions on any of the parameters so that the best fit value can be found for each parameter. The fit is performed again, but this time the observed spectrum is normalised by dividing it by the total of the template weights found from the previous fit. This will result in the total of all of the parameters being equal to 1, making it easy to alter their values.

The next step is to re-scale the errors on the observed SED so that we are assuming a good fit. A good fit requires that the value of  $\chi^2$  is equal to the number of degrees of freedom or, equivalently, that the reduced  $\chi^2$ ,  $\chi^2_{red}$ , is equal to 1. Since  $\chi^2_{red} = \chi^2_{best}/\nu$ , where  $\nu$  is the number of degrees of freedom, the errors can be re-scaled by first finding the variance of the residuals of the fit,  $\varepsilon$ . The residuals are given by

$$\varepsilon_i = O_i - E_i \quad (5.1)$$

where  $O_i$  is the  $i^{th}$  observed data point and  $E_i$  is the corresponding data point predicted by the model for the best fit parameters. If the fit is good, the model should just pass through the error bars for each data point, it follows that, if this is the case the variance of the residuals,  $\sigma^2(\varepsilon/\sigma)$ , will be equal to  $\chi^2_{red}$ .

$$\frac{\chi^2_{best}}{\nu} = \sigma^2 \left( \frac{\varepsilon}{\sigma} \right) \quad (5.2)$$

since each degree of freedom should contribute one standard deviation, so the average value of  $O_i - E_i/\sigma$  should be approximately 1. Dividing the errors for the SED by  $\sqrt{\sigma^2(\varepsilon/\sigma)}$  will ensure that  $\chi^2_{best} = \chi^2_{red}$ .

Now that the errors have been re-scaled and the SED has been normalised, we create a grid of values for each parameter, these are most concentrated around the best fit value and more sparsely sampled further away where the likelihood is small. For each value in the grid, a new fit is performed with the specified parameter set at that value. Values are fixed by passing different bounds to the solver used by GANDALF.

GANDALF makes use of Bounded Variables Least Squares Solver (BVLS) by Lawson and Hanson. BVLS is a FORTRAN library which solves the least squares problem  $\mathbf{A} \cdot \mathbf{X} = \mathbf{B}$ . In our case,  $\mathbf{A}$  is the set of treated templates,  $\mathbf{X}$  an array containing the

weights and  $\mathbf{B}$  is the observed spectrum. Within BVLS, the values of  $\mathbf{X}$  are subject to the condition

$$\text{BND}(0, j) \leq \mathbf{X}(j) \leq \text{BND}(1, j) \quad (5.3)$$

where  $\text{BND}$  is a  $2 \times j$  matrix containing the upper and lower bounds for the  $j$  parameters. A parameter can be fixed to a certain value by setting the upper and lower values of  $\text{BND}$  for some value of  $j$  to the desired value.

Essentially the error on each parameter is found using a brute-force grid of parameter values. The best value of  $\chi^2$ ,  $\chi^2_{best}$  is evaluated at each point on the grid. The only assumption made with this method is that the distribution of errors for the observed data is correct so that the likelihood function is correct (Andrae, 2010; Myung, 2003), however it has the disadvantage of being time consuming, since a fit needs to be performed for each point on the grid.

Starting with Bayes theorem and assuming a Gaussian distribution for the observed errors, we find that the natural logarithm of the probability of obtaining the observed data points,  $O$ , given model data points.  $E$ , is equivalent to  $\ln(\mathcal{L}) = K - \frac{\chi^2}{2}$ , where  $K$  is a constant and unimportant. This gives the likelihood,  $\mathcal{L}$ , for the parameter  $\theta$  with value  $x$  as

$$\mathcal{L}(\theta | x) = \exp\left(\frac{-\chi^2}{2}\right) \quad (5.4)$$

The cumulative distribution function (CDF) of the likelihood is given by the prefix sum of the likelihoods divided by their total.

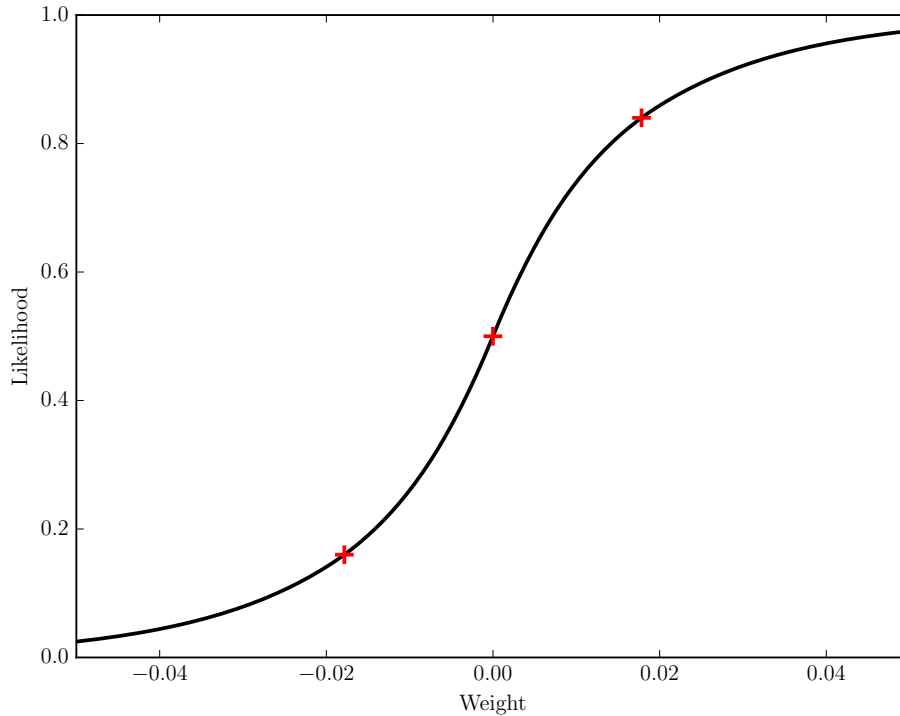
$$\frac{[\mathcal{L}_1, (\mathcal{L}_1 + \mathcal{L}_2), \dots, (\mathcal{L}_1 + \mathcal{L}_2 + \dots + \mathcal{L}_n)]}{\Sigma(\mathcal{L})} \quad (5.5)$$

The CDF can then be used to find the  $1\sigma$  error for each parameter. The  $1\sigma$  error is given by the percentage of values that lie within one standard deviation of the mean. This is equivalent to saying the  $1\sigma$  error is given by the values of  $x$  within which 68% of the probability is enclosed, i.e. the probability that  $x$  lies in the range  $\mu - \sigma \leq x \leq \mu + \sigma$  is 68%. These values of  $x$  are just the points where the CDF has a value of 16 and 84.

The 16 and 84 percentile values were found by interpolating between points. Accuracy could have been improved by fitting a function to the distribution of  $\chi^2$  values and then constructing the CDF, however their distribution was often too irregular to reliably fit a function to. Instead the  $\chi^2$  values were interpolated between linearly.

Figures 5.1 shows some of the resulting cumulative distribution functions for 2 of the parameters.

$Z = 0.05, t = 8.91\text{Gyrs}$



$Z = 0.004, t = 100\text{Myrs}$

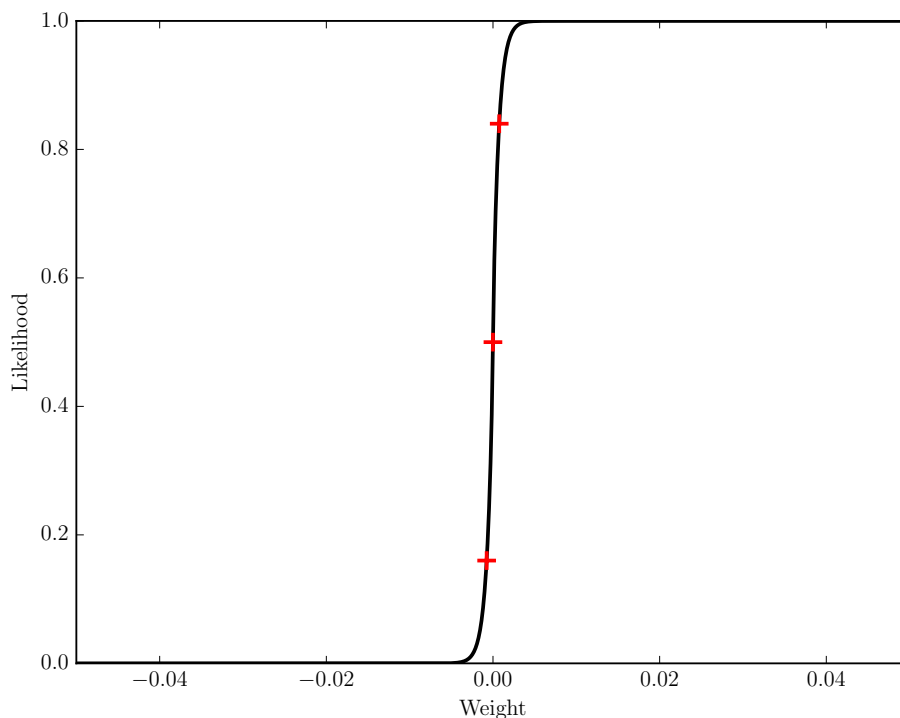


Figure 5.1: Some example cumulative distribution functions calculated from the  $\chi^2$  grid for various weights. The red crosses are placed at the points where the likelihood is equal to 0.14, 0.5 and 0.86. This gives the  $\sigma$  error.

After the errors for each parameter were found, the best fits and their errors were split into young, intermediate and old population bins. These span  $t \leq 100$ Myrs for populations considered young,  $100\text{Myrs} < t \leq 2\text{Gyrs}$  for intermediate populations and  $t > 2\text{Gyrs}$  old populations. Figures 5.2 and 5.3 show the parameters values for each weight, they also show the total weight in each bin and its error, calculated from the quadratic sum of the errors in that bin. This provides an easy way of viewing the distribution of stellar populations in terms of age while also giving an idea of their uncertainty.

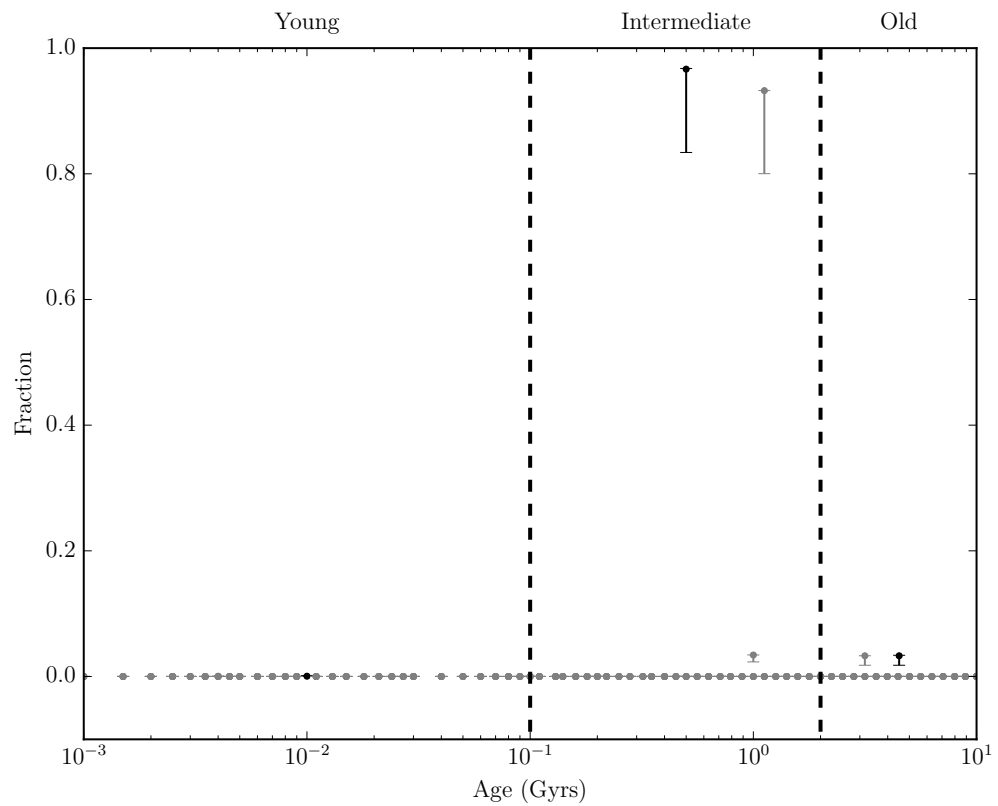


Figure 5.2: Weights with error bars obtained for the bulge of NGC 7742. The individual weights and their errors are shown in grey and the binned weights and errors are shown in black. The  $x$  position of the points in black is arbitrary (the centre of their bin).

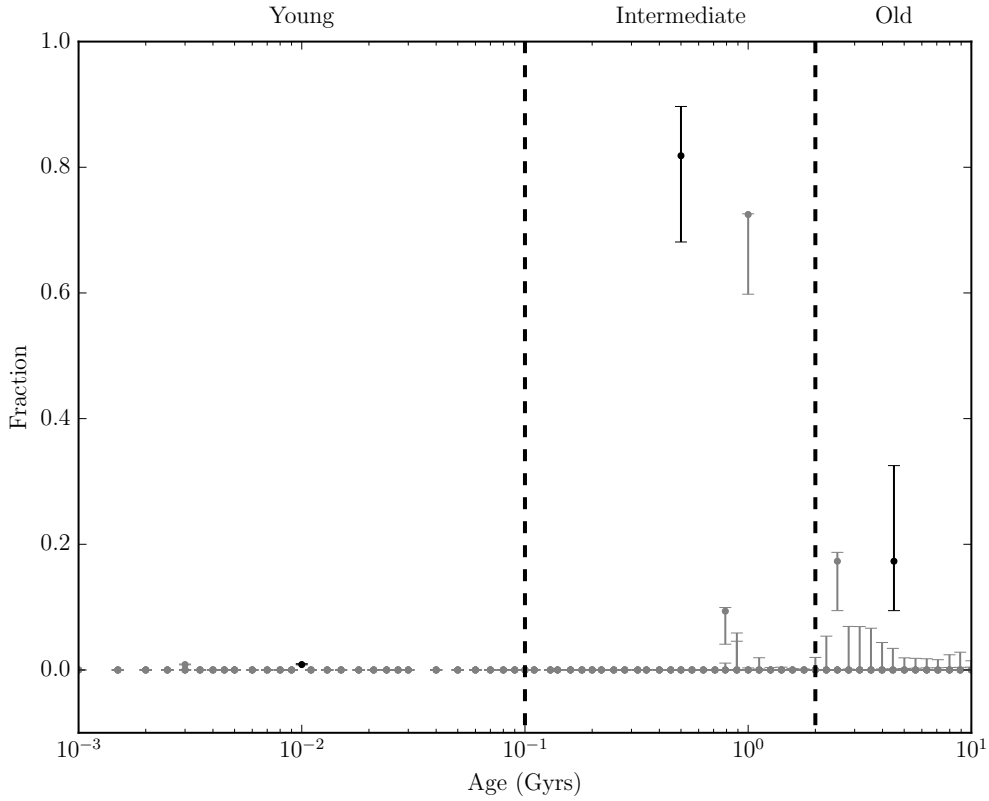


Figure 5.3: Weights with error bars obtained for the ring of NGC 7742. The individual weights and their errors are shown in grey and the binned weights and errors are show in black.

The plots seem to indicate that young populations are best constrained in terms of their error. This is likely because of the high luminosity of young populations compared with their mass. This means that a small change in the template weight for a young SSP will result in a larger change in flux density, since the templates are mass normalised.

## 6 Conclusion

This project concerned verification of a spectro-photometric approach to SED fitting in order to reconstruct the star-formation history of galaxies. The focus was on a test-case galaxy, NGC 7742. A face-on Sa galaxy, host to a starburst ring. The aim was to test this approach by altering existing SED fitting code and then comparing the results with SED fits utilising spectroscopic-only and photometric-only SEDs for NGC 7742.

In §1, some of the basic principles of SED fitting were introduced. The history of the study of stellar populations and of early approaches to SED fitting were discussed. Elements and techniques necessary to the process of recovering star formation history were reviewed: stellar population synthesis was discussed as was the importance of simple stellar populations as the building blocks for models of galactic SEDs. Also reviewed were spectroscopic and photometric observations, SED fitting using  $\chi^2$  minimisation to estimate the distribution of stellar populations in age and metallicity as well as necessary treatment of template SSPs when fitting including reddening and convolution with stellar kinematics.

§2 concerned the available data for NGC 7742. The properties of MUSE, GALEX and SDSS instruments were discussed as well as the properties of the data themselves. The calibration of the data into units of wavelength dependent spectral flux density and also the process of obtaining errors on these flux densities was described. The properties of the GALEXEV SSP library were detailed and their suitability for the purpose of recovering star-formation histories using MUSE spectra were justified.

In §3, the functioning of the GANDALF SED fitting code was described. The way that apertures were chosen and extracted from the data was described and values obtained for the flux density in each band for each aperture were presented with their errors. The methods used treat the data and modify the SED fitting code were described. The point spread function for each image was determined by fitting a Gaussian to a point source in the image, the images and the MUSE datacube were then convolved with a Gaussian such that they were degraded to the same angular resolution. The method by which the photometric fluxes were calculated for each GALEXEV template were detailed and changes to the GANDALF code described. Finally the method by which additional reddening for young stellar templates is applied within GANDALF using the  $E(B - V)_{\text{internal}}$  parameter was illustrated.

The results of the GANDALF SED fits using only photometry and only the MUSE spectrum were presented. It was found that the fit to photometry suffered severely from reddening-age degeneracy, since there are no 'hooks' like the Balmer decrement in the photometry that allow the  $E(B - V)$  values to be found. This resulted in very unphysical fits.

§4 concerned the final fit using the extended spectro-photometric approach. Fits were made to an SED comprised of both photometric and spectroscopic data points and these fits were then compared with the fits to the spectrum only. It was found that introducing photometric data points did not alter the  $\chi^2$  for the goodness of fit to the spectrum by any more than 0.05%, indicating that the fit to the spectrum is not worsened by also fitting to the photometric points. It was found that there were significant differences between the spectroscopic fit and the spectro-photometric fit. It was found that the spectroscopic fit over or underestimated the flux in the UV. This indicates that there is information regarding the UV bright populations present in the UV data points that is not present in the optical-only spectrum. So UV data is required to better constrain the UV flux and thus young, UV bright SSPs.

In §5, the process of obtaining errors on the best fit parameters was described and errors were presented. Parameters were varied according to a grid of values. The NGC 7742 spectro-photometric SED was refit, keeping one of the parameters constant each time. This produces a distribution of  $\chi^2$  as a function of the parameter value for each parameter. Using the  $\chi^2$  values to compute a likelihood for each point, a cumulative distribution function was plotted for each parameter which was used to find the  $1\sigma$  error. Parameter values were presented with their corresponding errors binned into young, intermediate and old age populations.

This project has shown that, in the case of NGC 7742, SED fitting the using optical MUSE spectrum fails to predict the observed ultraviolet flux density and, therefore, the UV bright young stellar population. The addition of GALEX data allows the model SED to be matched in the UV with the observed UV flux density, better constraining star formation history for young SSPs.

It would be interesting to repeat error analysis for the spectrum only fit. This would make it possible to confirm whether there is a statistically significant difference between the parameter values obtained using the spectroscopic and spectro-photometric approaches. It would also be interesting to see if the GALEX data allows the parameter values to be better constrained, which would result in a smaller error for the spectro-photometric approach if true.

It might also be useful to repeat the error analysis using a revised grid of parameter values. By considering the distribution of the  $\chi^2$  for each parameter individually, a grid could be produced that better samples that distribution. This would produce better error estimates because it would be possible to ensure that interpolation between points does not badly change the distribution.

Errors obtained for the MUSE spectrum and GALEX photometry need to be investigated further. For the disk of NGC 7742, it was found that the best-fit model SED did not pass through the GALEX data points. It is possible that calibration errors are

not folded into the MUSE datacube, resulting in a artificially small error for MUSE compared with GALEX or that the MUSE errors are underestimated at the edges of the galaxy, resulting in the GALEX data points being under-fitted.

The combined spectro-photometric SED fitting method could be applied to data for other galaxies, especially galaxies of different types. It would then be possible to compare spectroscopic fit with the spectro-photometric fit for a wide range of data, so that the true extent of the mismatch between the two types of fit could be quantified.

After the approach has been tested fully, it would be especially useful for exploring star-formation efficiency throughout galaxies. The star-formation rate and gas fraction could be calculated across the spatial extent of the galaxy, making it possible to produce maps of star-formation efficiency. Another more general application would be the ability to achieve more accurate SED fitting for limited spectra with the addition of photometry. With the advent of large, multiwavelength sky surveys, photometric data has become plentiful, so it is likely that a considerable body of photometric data will be available for any objects of interest.

The new MaNGA integral field spectroscopic survey (Bundy et al., 2015), part of the fourth generation Sloan Digital Sky Survey will produce large wavelength coverage (3600Å to 10300Å) spectroscopy of nearby galaxies, albeit at lower angular resolutions than MUSE. The new data produced by MaNGA will be ideal for use with the spectro-photometric technique that has been developed.

## References

- René Andrae. Error estimation in astronomy: A guide. *arXiv preprint arXiv:1009.2755*, 2010.
- W Baade. NGC 147 and NGC 185, two new members of the local group of galaxies. *The Astrophysical Journal*, 100:147, 1944.
- R Bacon, M Accardo, L Adjali, H Anwand, S Bauer, I Biswas, J Blaizot, D Boudon, S Brau-Nogue, J Brinchmann, et al. The MUSE second-generation VLT instrument. In *SPIE Astronomical Telescopes+ Instrumentation*, pages 773508–773508. International Society for Optics and Photonics, 2010.
- Luciana Bianchi. The galaxy evolution explorer (galex). its legacy of uv surveys, and science highlights. *Astrophysics and Space Science*, 354(1):103–112, 2014.
- G Bruzual and S Charlot. GALEXEV (version 2003). Online, 2003a.
- G Bruzual and S Charlot. Stellar population synthesis at the resolution of 2003. *Monthly Notices of the Royal Astronomical Society*, 344(4):1000–1028, 2003b.
- Kevin Bundy, Matthew A Bershady, David R Law, Renbin Yan, Niv Drory, Nicholas MacDonald, David A Wake, Brian Cherinka, José R Sánchez-Gallego, Anne-Marie Weijmans, et al. Overview of the sdss-iv manga survey: Mapping nearby galaxies at apache point observatory. *The Astrophysical Journal*, 798(1):7, 2015.
- D. Calzetti. *Star Formation Rate Indicators*, page 419. October 2013.
- Daniela Calzetti. The dust opacity of star-forming galaxies. *Publications of the Astronomical Society of the Pacific*, 113(790):1449–1485, 2001.
- Daniela Calzetti, Anne L Kinney, and Thaisa Storchi-Bergmann. Dust extinction of the stellar continua in starburst galaxies: The ultraviolet and optical extinction law. *The Astrophysical Journal*, 429:582–601, 1994.
- Daniela Calzetti, Lee Armus, Ralph C Bohlin, Anne L Kinney, Jan Koornneef, and Thaisa Storchi-Bergmann. The dust content and opacity of actively star-forming galaxies. *The Astrophysical Journal*, 533(2):682, 2000.
- Michele Cappellari and Eric Emsellem. Parametric recovery of line-of-sight velocity distributions from absorption-line spectra of galaxies via penalized likelihood. *Publications of the Astronomical Society of the Pacific*, 116(816):138–147, 2004.

- Igor V. Chilingarian and Ivan Yu. Katkov. NBursts+phot: parametric recovery of galaxy star formation histories from the simultaneous fitting of spectra and broadband spectral energy distributions. In *The Spectral Energy Distribution of Galaxies*, volume 7 of *Proceedings of the International Astronomical Union*, pages 26–28, 9 2011.
- Daniel J Eisenstein, David H Weinberg, Eric Agol, Hiroaki Aihara, Carlos Allende Prieto, Scott F Anderson, James A Arns, Éric Aubourg, Stephen Bailey, Eduardo Balbinot, et al. Sdss-iii: Massive spectroscopic surveys of the distant universe, the milky way, and extra-solar planetary systems. *The Astronomical Journal*, 142(3):72, 2011.
- J. Fischera, M. A. Dopita, and R. S. Sutherland. Starburst Galaxies: Why the Calzetti Dust Extinction Law?
- J. E. Gunn, M. Carr, C. Rockosi, M. Sekiguchi, K. Berry, B. Elms, E. de Haas, Ž. Ivezić, G. Knapp, R. Lupton, G. Pauls, R. Simcoe, R. Hirsch, D. Sanford, S. Wang, D. York, F. Harris, J. Annis, L. Bartozek, W. Boroski, J. Bakken, M. Halde- man, S. Kent, S. Holm, D. Holmgren, D. Petravick, A. Protopiano, R. Rechenmacher, M. Doi, M. Fukugita, K. Shimasaku, N. Okada, C. Hull, W. Siegmund, E. Mannery, M. Blouke, D. Heidtman, D. Schneider, R. Lucinio, and J. Brinkman. The Sloan Digital Sky Survey Photometric Camera. *The Astronomical Journal*, 116:3040–3081, December 1998. doi: 10.1086/300645.
- M. R. Krumholz. Star formation in molecular clouds. In E. Telles, R. Dupke, and D. Lazzaro, editors, *American Institute of Physics Conference Series*, volume 1386 of *American Institute of Physics Conference Series*, pages 9–57, September 2011. doi: 10.1063/1.3636038.
- J-F Le Borgne, G Bruzual, R Pelló, A Lançon, B Rocca-Volmerange, B Sanahuja, D Schaefer, C Soubiran, and R Vílchez-Gómez. Stelib: A library of stellar spectra at  $r = 2000$ . *Astronomy & Astrophysics*, 402(2):433–442, 2003.
- C. Leitherer. Modeling the stellar spectral energy distributions of star-forming galaxies. In C. C. Popescu and R. J. Tuffs, editors, *The Spectral Energy Distributions of Gas-Rich Galaxies: Confronting Models with Data*, volume 761 of *American Institute of Physics Conference Series*, pages 39–58, April 2005. doi: 10.1063/1.1913914.
- Claus Leitherer. Modeling the stellar spectral energy distributions of star-forming galaxies. *arXiv preprint astro-ph/0411345*, 2004.

- D Christopher Martin, James Fanson, David Schiminovich, Patrick Morrissey, Peter G Friedman, Tom A Barlow, Tim Conrow, Robert Grange, Patrick N Jelinsky, Bruno Milliard, et al. The galaxy evolution explorer: A space ultraviolet survey mission. *The Astrophysical Journal Letters*, 619(1):L1, 2005.
- P. Massey and M. M. Hanson. *Astronomical Spectroscopy*, page 35. 2013.
- Patrick Morrissey, David Schiminovich, Tom A Barlow, D Christopher Martin, Brian Blakkolb, Tim Conrow, Brian Cooke, Kerry Erickson, James Fanson, Peter G Friedman, et al. The on-orbit performance of the galaxy evolution explorer. *The Astrophysical Journal Letters*, 619(1):L7, 2005.
- Patrick Morrissey, Tim Conrow, Tom A Barlow, Todd Small, Mark Seibert, Ted K Wyder, Tamás Budavári, Stephane Arnouts, Peter G Friedman, Karl Forster, et al. The calibration and data products of galex. *The Astrophysical Journal Supplement Series*, 173(2):682, 2007.
- In Jae Myung. Tutorial on maximum likelihood estimation. *Journal of mathematical Psychology*, 47(1):90–100, 2003.
- RW O’Connell. Galaxy spectral synthesis. i-stellar populations in the nuclei of giant ellipticals. *The Astrophysical Journal*, 206:370–390, 1976.
- R. F. Peletier. *Stellar Populations*, page 353. October 2013.
- J Richard and R Bacon. MUSE User Manual. Online, 2015.
- Wallace LW Sargent, Paul L Schechter, A Boksenberg, and Keith Shorridge. Velocity dispersions for 13 galaxies. *The Astrophysical Journal*, 212:326–334, 1977.
- M. Sarzi, J. Falcón-Barroso, R. L. Davies, R. Bacon, M. Bureau, M. Cappellari, P. T. de Zeeuw, E. Emsellem, K. Fathi, D. Krajnović, H. Kuntschner, R. M. McDermid, and R. F. Peletier. The SAURON project - V. Integral-field emission-line kinematics of 48 elliptical and lenticular galaxies. *MNRAS*, 366:1151–1200, March 2006.
- Ricardo P. Schiavon. History of star formation of early type galaxies from integrated light: clues from stellar ages and abundances, 2010.
- Leonard Searle, WLW Sargent, and WG Bagnuolo. The history of star formation and the colors of late-type galaxies. *The Astrophysical Journal*, 179:427–438, 1973.

- Eline Tolstoy, Vanessa Hill, and Monica Tosi. Star formation histories, abundances and kinematics of dwarf galaxies in the local group. *arXiv preprint arXiv:0904.4505*, 2009.
- Jakob Walcher, Brent Groves, Tams Budavari, and Daniel Dale. Fitting the integrated spectral energy distributions of galaxies, 2010.